NAVAL POSTGRADUATE SCHOOL

MONTEREY, CALIFORNIA

THESIS

DESIGN AND DEVELOPMENT OF A SINGLE CHANNEL RSNS DIRECTION FINDER

by

Jessica A. Benveniste

March 2009

Thesis Co-Advisors: Phillip E. Pace
David C. Jenn

Approved for public release; distribution is unlimited

THIS PAGE INTENTIONALLY LEFT BLANK

REPORT DOCUMENTATION PAGE		Form Approved OMB No. 0704-0188

1. AGENCY USE ONLY *(Leave blank)*	2. REPORT DATE March 2009	3. REPORT TYPE AND DATES COVERED Master's Thesis

4. TITLE AND SUBTITLE Design and Development of a Single Channel RSNS Direction Finder	5. FUNDING NUMBERS
6. AUTHOR(S) Jessica A. Benveniste	
7. PERFORMING ORGANIZATION NAME(S) AND ADDRESS(ES) Naval Postgraduate School Monterey, CA 93943-5000	8. PERFORMING ORGANIZATION REPORT NUMBER
9. SPONSORING /MONITORING AGENCY NAME(S) AND ADDRESS(ES) N/A	10. SPONSORING/MONITORING AGENCY REPORT NUMBER

11. SUPPLEMENTARY NOTES The views expressed in this thesis are those of the author and do not reflect the official policy or position of the Department of Defense or the U.S. Government.

12a. DISTRIBUTION / AVAILABILITY STATEMENT Approved for public release; distribution is unlimited	12b. DISTRIBUTION CODE

13. ABSTRACT (maximum 200 words)

This thesis carried out the design and development of a single channel Robust Symmetrical Number System (RSNS) virtual spacing direction finding (DF) system. This was based on previous work on a three-channel RSNS virtual spacing DF system. Various moduli sets were chosen and run through MATLAB simulations. The results showed unacceptably large errors at low signal-to-noise ratios (SNRs) for all sets. Large dynamic range moduli sets yielded relatively high errors when compared with the small dynamic range moduli sets. The effect of number of channels was studied and found to be mostly inconsequential for similar resolutions. The simulation included phase errors from noise and spacing errors. The virtual single channel concept was integrated into a hardware system. A bench top setup with amplifier and demodulator cards was constructed. This system was connected to two National Instruments (NI) PXI-5112 cards. LabVIEW software was used to calibrate the demodulator cards and to run the RSNS program.

14. SUBJECT TERMS Direction Finding, Robust Symmetrical Number System, Single Channel, Angle of Arrival	15. NUMBER OF PAGES 95
	16. PRICE CODE

17. SECURITY CLASSIFICATION OF REPORT	18. SECURITY CLASSIFICATION OF THIS PAGE	19. SECURITY CLASSIFICATION OF ABSTRACT	20. LIMITATION OF ABSTRACT
Unclassified	Unclassified	Unclassified	UU

NSN 7540-01-280-5500 Standard Form 298 (Rev. 8-98)
Prescribed by ANSI Std. Z39.18

THIS PAGE INTENTIONALLY LEFT BLANK

Approved for public release; distribution is unlimited

DESIGN AND DEVELOPMENT OF A SINGLE CHANNEL RSNS DIRECTION FINDER

Jessica A. Benveniste
Civilian, Department of the Air Force
B.S., Boston University, 2003

Submitted in partial fulfillment of the
requirements for the degree of

MASTER OF SCIENCE IN ELECTRICAL ENGINEERING

from the

NAVAL POSTGRADUATE SCHOOL
March 2009

Author: Jessica A. Benveniste

Approved by: Phillip E. Pace
Thesis Co-Advisor

David C. Jenn
Thesis Co-Advisor

Jeffrey B. Knorr
Chairman, Department of Electrical and Computer Engineering

THIS PAGE INTENTIONALLY LEFT BLANK

ABSTRACT

This thesis carried out the design and development of a single channel Robust Symmetrical Number System (RSNS) virtual spacing direction finding (DF) system. This was based on previous work on a three-channel RSNS virtual spacing DF system. Various moduli sets were chosen and run through MATLAB simulations. The results showed unacceptably large errors at low signal-to-noise ratios (SNRs) for all sets. Large dynamic range moduli sets yielded relatively high errors when compared with the small dynamic range moduli sets. The effect of number of channels was studied and found to be mostly inconsequential for similar resolutions. The simulation included phase errors from noise and spacing errors. The virtual single channel concept was integrated into a hardware system. A bench top setup with amplifier and demodulator cards was constructed. This system was connected to two National Instruments (NI) PXI-5112 cards. LabVIEW software was used to calibrate the demodulator cards and to run the RSNS program.

THIS PAGE INTENTIONALLY LEFT BLANK

TABLE OF CONTENTS

THIS PAGE INTENTIONALLY LEFT BLANK

LIST OF FIGURES

LIST OF TABLES

THIS PAGE INTENTIONALLY LEFT BLANK

EXECUTIVE SUMMARY

Radio direction finding (DF) has been used in navigation and military applications for many years. It requires amplitude comparison, phase delay, or time delay to calculate the angle of arrival (AOA) of a signal. Amplitude comparison uses the directional amplitude response of an antenna to acquire the AOA of the signal. Phase and time delay systems obtain the AOA information using phase and time of arrival [1], respectively. Both of these methods require the use of at least two antenna separated by a known spacing, d which is referred to as the baseline. Ambiguities can become a problem as higher resolution is desired. When the element spacing grows beyond half the wavelength more than one AOA result can occur. Other techniques have been used to try to overcome the problem, such as increasing the baseline, extended phase interferometry, and symmetric pair antenna. Some are complex and others impractical.

This thesis carried out the design and development of a single channel Robust Symmetrical Number System (RSNS) [10] virtual spacing DF system. RSNS uses moduli in an interferometer setup to symmetrically fold the phase differences. Previous experimental results have shown much success therefore this work modified and extended previous research.

This study focused on SNR variations for 2, 3, and 4 channel dynamic range values ($\widehat{M}$). Various moduli sets were chosen of small, medium, and large values and run through MATLAB simulations. While errors were large at low SNRs, the high SNR data for all moduli sets proved the single channel virtual concept worked as desired. The effect of number of channels was studied and found to be mostly inconsequential. The most favorable results were achieved for a dynamic range value of $\widehat{M} = 85$.

A straight forward application of the RSNS processing requires a pair of elements per RSNS modulus. A single channel processing approach was developed where the data for all moduli can be obtained from a single pair of elements.

The virtual single channel processor was integrated into a hardware system. This consisted of a frequency source, various power splitters, phase shifters, demodulator boards, amplifiers, and low pass filters. The system was connected to two National Instruments (NI) PXI-5112 digital oscilloscope cards. LabVIEW software was used for the calibration and RSNS processing. The phase shifters were used to simulate plane wave incidence at various angles. The AOA results behaved as expected.

ACKNOWLEDGMENTS

I would like to thank my husband, Steven Benveniste, without who's help and encouragement, I would have not made it this far.

I would like to thank my advisors, Professor Phillip E. Pace and Professor David C. Jenn for their wise guidance through this process. I have learned so much throughout my time at NPS. Their incredible patience and assistance as I stumbled through concepts and problems was valued and respected greatly.

I would also like to thank Mr. Robert D. Broadston, Lab Director for the ECE Microwave Lab. I appreciate all the time he spent making and setting up equipment and helping me to understand the hardware and test equipment. His troubleshooting skills and expert experience were essential to my success.

A special thanks to my family and friends without whom the craziness of school may just have overwhelmed me completely.

THIS PAGE INTENTIONALLY LEFT BLANK

I. INTRODUCTION

A. DIRECTION FINDING

Radio Direction Finding (DF) is a method by which the direction of arrival, or angle of arrival (AOA), of an electromagnetic wave is found [1]. Radio DF has been used in navigation and military applications for many years.

DF systems can calculate the AOA in three different ways: amplitude comparison, phase delay, or time delay. Amplitude comparison uses the directional amplitude response of an antenna to acquire the AOA of the signal. Phase and time delay systems obtain the AOA information using phase and time of arrival, respectively [1]. Both of these methods require the use of at least two antennas separated by a known spacing, d, which is referred to as the baseline. Figure 1 displays a single array with an illustration of an incident plane wave arriving at the antenna elements.

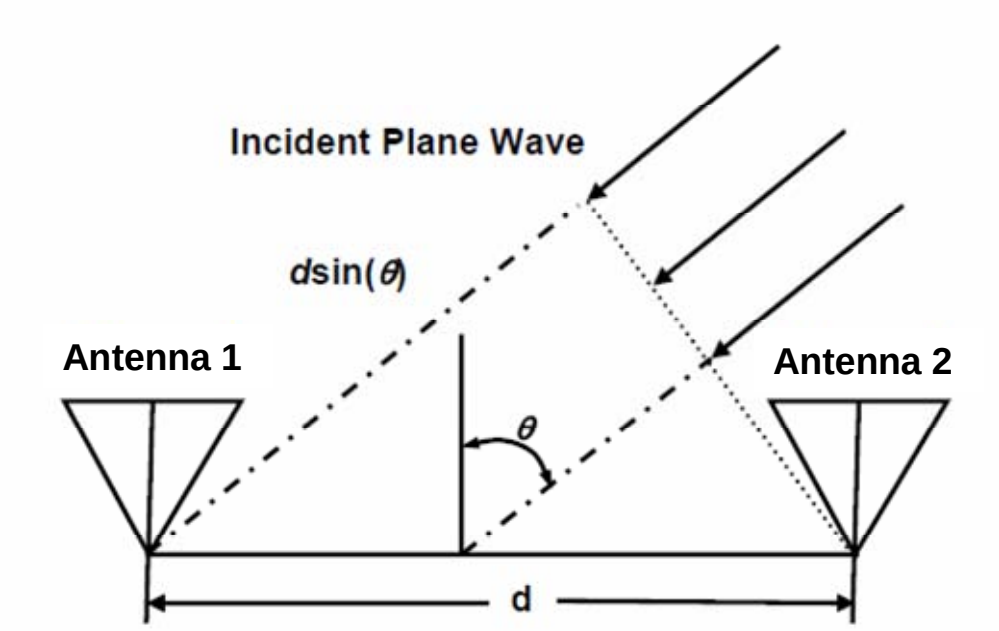

Figure 1. Interferometer Illustration (After [2])

In the case of phase interferometry, the impinging wave on an ideal interferometer will have the same amplitude at both antenna elements [3]. Direction information is then contained entirely in the phase measured at the antenna elements. In some applications a high resolution is desired which, in general, can be achieved through increasing the element spacing. Ambiguities can be introduced in this process when the element spacing is increased beyond the half wavelength distance. This can result in more than one AOA result.

To resolve the ambiguities, an additional interferometer, or additional elements, can be added [3]. Adding additional elements or increasing baselines, can be favorable as it can increase resolution; however too large of a baseline has high space requirements.

Other approaches have been investigated to alleviate this problem. Another technique called extended phase interferometry [4] uses calibrated phase and amplitude response data from the antenna elements. It weights the square of the baseline phase differences with antenna gains.

A low-resolutions phase measurement technique, symmetric pair antenna array [5], is another way to gain a more accurate DF. The antenna array relies on symmetry about a pair of antenna array. The symmetric pair antenna array uses measured polarities for azimuth and elevation angles.

B. PREVIOUS WORK

The Robust Symmetrical Number System (RSNS) is a modular preprocessing architecture which has been used for both analog and digital signal processing. Integer values within moduli sets change one at a time to the next position as in a gray-code sequence. The RSNS is popular due to the error control properties [6].

Research into the RSNS for DF has been studied due to the potential it presents to decrease the antenna baseline while increasing the resolution. Research was accomplished on a three-channel RSNS array in a previous thesis

with reasonable results. Past work included an analog architecture that was built using a four-inch antenna array. This architecture had an angular resolution of 1.8° at 8 GHz as described in [7]. A digital architecture using quadrature demodulators was designed and two four-element hardware setups were produced. One of the arrays produced 0.7° resolution at 2.4 GHz as described in [2]. The virtual concept was introduced in [4] including a study of noise effects. A virtual RSNS concept was simulated and showed an increase in performance and error handling. The virtual RSNS concept requires only a single pair of elements to achieve an arbitrary resolution in the absence of noise.

C. PRINCIPAL CONTRIBUTIONS

This thesis focused on the design and analysis of a single-channel virtual spacing DF system. The primary contribution is simulation and verification of the single-channel virtual spacing concept.

The single-channel virtual spacing concept was to be used to process quadrature data from a two-element antenna array. The hardware for this thesis did not include the antenna elements, but stopped short with a fixed phase radio frequency (RF) input and a phase shifted RF input to two sets of demodulator boards. The demodulator boards then passed the data through a differential amplifier and a low pass filter (LPF) then fed the quadrature data to the National Instruments (NI) PXI-5112 Digital Oscilloscope cards. Once this data was received in a LabVIEW program, the RSNS portion of the program ran to yield AOA estimates based on the phase difference between the two demodulator boards.

Simulations were done with modifications to a MATLAB code from [5]. The MATLAB code employed the signal-channel concept. Spacing errors, phase errors, and frequency errors were taken into consideration in the simulations. Multiple sets of moduli were simulated and statistically compared with consideration given to scale factor and field of view. Each moduli set was simulated for a range of signal-to-noise (SNR) values from 10 dB to 50 dB and

were run 25 times for each point. Root mean square (RMS) error values were calculated for each SNR value and each moduli set.

Calibration measurements were made on the demodulator boards by gathering quadrature measurements over a 360° range and averaging the values to find the center of the resulting circle. These I and Q values were then set as the offset values for the next step of hardware testing.

One set of moduli was used during the hardware phase of the thesis and integrated into a LabVIEW program. A synchronization program for the two NI PXI-5112 Digital Oscilloscope cards was used at the beginning of the program. The data was averaged for a fixed phase difference and $10,000$ points then fed into the RSNS algorithm within LabVIEW, based on the MATLAB script in the previous work.

D. THESIS OUTLINE

Chapter II reviews the basic operating principles of Radio DF systems and applies the basics for RSNS direction finding.

Chapter III explains RSNS theory and applications with a design example included.

Chapter IV provides the simulation and results.

Chapter V explains the test procedures and evaluation of test results is presented.

Chapter VI contains concluding remarks and suggestions for future research efforts.

II. PHASE INTERFEROMETRY

This chapter reviews the basic concepts of DF by use of phase interferometry.

A. THEORY

In DF the common assumption is that the antenna operates in the far field of the emitter. This assumption allows analysis to be completed using a plane wave. A diagram of a one channel interferometer setup is shown in Figure 2. The angle of arrival for a signal is limited to $\pm 90^{\circ}$. In the figure, the signal arrives at antenna 2 and continues through the distance $d\sin(\theta)$ to antenna 1.

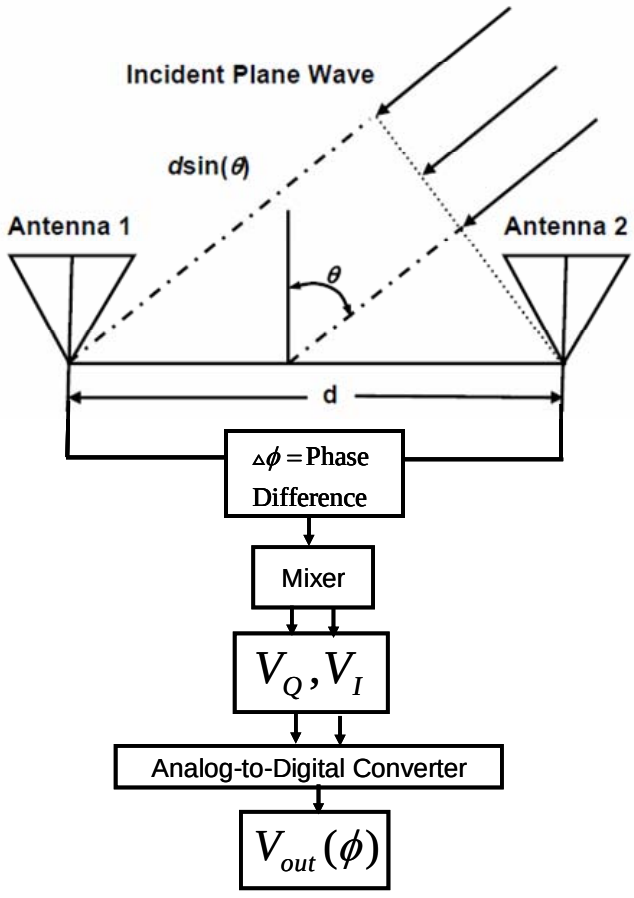

Figure 2. Interferometer Setup with RSNS Moduli (After [2])

The received signal at the output of the antenna is of the following form

$$V_i = V\cos(\omega_c t + \psi_i + \phi_i) \tag{2.1}$$

where i is the element index number, V_i is the signal amplitude response, ω_c is the signal frequency in radians/second, ψ_i is the phase due to cables, and ϕ_i is the phase due to path delay relative to antenna 1, which is the reference. After the signal has moved through the phase detector elements, which can be modeled as mixing with the carrier frequency and then filtering, the output voltage is given as

$$V_{out}(\phi) = \frac{V^2}{2}\cos(\triangle\psi + \triangle\phi). \tag{2.2}$$

The phase, $\triangle\psi$, is known by measuring the phase shift in the cables and $\triangle\phi$ can be determined from the measured phase difference between the elements. This value is written as

$$\triangle\phi = \phi_2 - \phi_1 = kd\sin(\theta) \tag{2.3}$$

where $k = \frac{2\pi}{\lambda}$ is defined as the wave number and λ is the wavelength.

Combining Equations (2.2) and (2.3), assuming $\triangle\psi$ is known and subtracted out, the output voltage can now be displayed as

$$V_{out}(\phi) = \cos(kd\sin(\theta)). \tag{2.4}$$

Therefore, once the phase difference between elements is measured, the information can be passed on to the RSNS moduli where it is processed and the resulting AOA is output.

B. QUADRATURE DEMODULATION

Quadrature demodulation is a primary focus in the data processing of a digital DF system [8]. A bandpass signal is expressed as

$$x_{band}(t) = x_I\cos(\omega_c t) - x_Q\sin(\omega_c t) \tag{2.5}$$

where $\omega_c = 2\pi f_c$, f_c is the carrier frequency,

x_I is the in-phase component, and

x_Q is the quadrature component.

The output voltage can be expressed as

$$V(p_n,t) = \mathrm{Re}\left(A(p_n)e^{j(\omega_c t)}\right) \tag{2.6}$$

where p_n is the position at the antenna element, Re is the real operator, and $n = 1,2$ is the antenna element index. From [8] $A(p_n)$ is

$$A(p_n) = \left|A(p_n)\right|e^{j\phi(p_n)} = A_I(p_n) + jA_Q(p_n)\,. \tag{2.7}$$

The quadrature voltages once the signal has gone through the mixers are

$$V_I = V(p_n,t)\cos(\omega_c t) = \frac{1}{2}A_I(p_n) + \frac{1}{2}\left[A_I(p_n)\cos(2\omega_c t) - A_Q(p_n)\sin(2\omega_c t)\right], \tag{2.8}$$

$$V_Q = -V(p_n,t)\sin(\omega_c t) = -\frac{1}{2}\left[A_I(p_n)\sin(2\omega_c t) + A_Q(p_n)\cos(2\omega_c t)\right] + \frac{1}{2}A_Q(p_n)\,. \tag{2.9}$$

The signal is next passed through a low pass filter (LPA) and those voltages are

$$V_I(p_n) = \frac{1}{2}A_I(p_n) = \frac{1}{2}\left|A(p_n)\right|\cos(\phi(p_n))\,, \tag{2.10}$$

$$V_Q(p_n) = \frac{1}{2}A_Q(p_n) = \frac{1}{2}\left|A(p_n)\right|\sin(\phi(p_n))\,. \tag{2.11}$$

For a plane wave it is assumed that $\left|A(p_n)\right| = 1$

$$V_{In} = V_I(p_n) = \cos(\phi(p_n)) \tag{2.12}$$

$$V_{Qn} = V_Q(p_n) = \sin(\phi(p_n)) \tag{2.13}$$

These voltages are used to calculated the phase differential term between the antenna elements 1 and 2

$$\triangle\phi_{12} = \phi_1(p_n) - \phi_2(p_n) = \arctan\left(\frac{V_{Q1}}{V_{I1}}\right) - \arctan\left(\frac{V_{Q2}}{V_{I2}}\right) = kd_1\sin\theta \tag{2.14}$$

where d_1 is the distance between the antenna elements.

An analog-to-digital converter (ADC) digitizes the I and Q values and an equivalent voltage folding waveform is obtained using Equation (2.4). The cosine of the phase differential in Equation (2.14) yields

$$V_{out}(\phi) = \cos(kd_1 \sin(\theta)) = \cos(\triangle\phi_{12}) . \quad (2.15)$$

The RSNS is mapped to the folding waveform as described in Chapter III.

C. AMBIGUITY

As stated in Chapter I, an ambiguity can occur if the element spacing exceeds half of a wavelength. This ambiguity will be illustrated by comparing two examples. First, in Figure 3 the antenna element spacing is $d = \frac{\lambda}{2}$ which shows the mapping of phase difference and AOA without ambiguities. The spacing leads to a phase difference using Equation (2.3) of $\triangle\phi = \pi \sin(\theta)$.

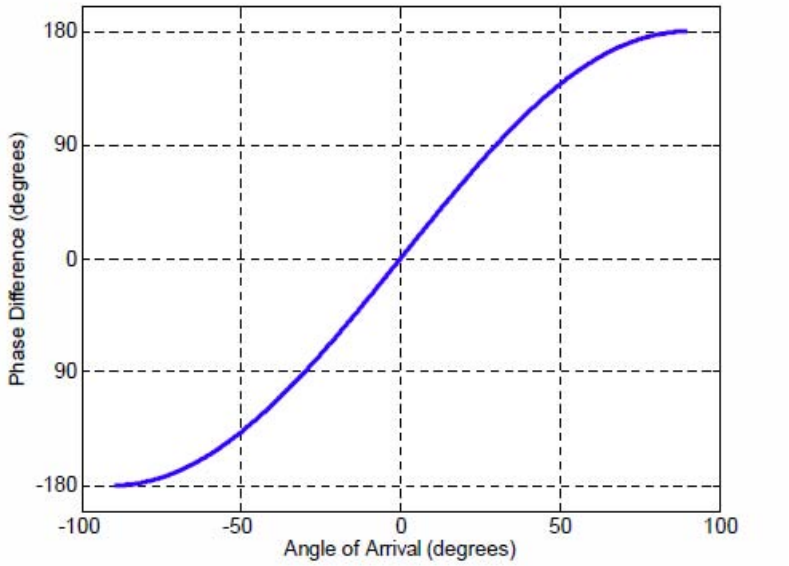

Figure 3. Phase Differential vs AOA for $d = \frac{\lambda}{2}$ (From [2])

For spacing $d \geq \frac{\lambda}{2}$ an ambiguity will occur. If $d = \lambda$, using Equation (2.3) again, $\triangle\phi = 2\pi \sin(\theta)$. From this equation, there is expected to be 2 solutions for the AOA given one phase difference. This is illustrated in Figure 4.

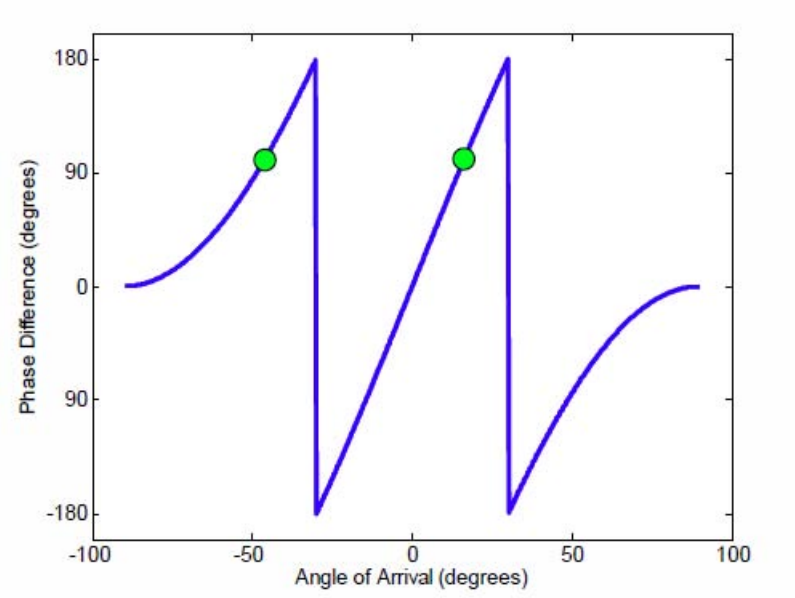

Figure 4. Phase Differential vs AOA for $d = \lambda$ (From [2])

D. FOLDING WAVEFORMS

From the examples for $d = \frac{\lambda}{2}$ and $d = \lambda$, the output voltage can be plotted versus AOA. Figure 5 provides this illustration and from it the symmetric development for AOAs between $\pm 90^{\circ}$ is seen. As explained from the previous section, there is a single fold for the $d = \frac{\lambda}{2}$ AOA values, while the $d = \lambda$ AOA values create two folds. The number of folding periods, n, is given by

$$n = \frac{d}{\lambda / 2}. \tag{2.16}$$

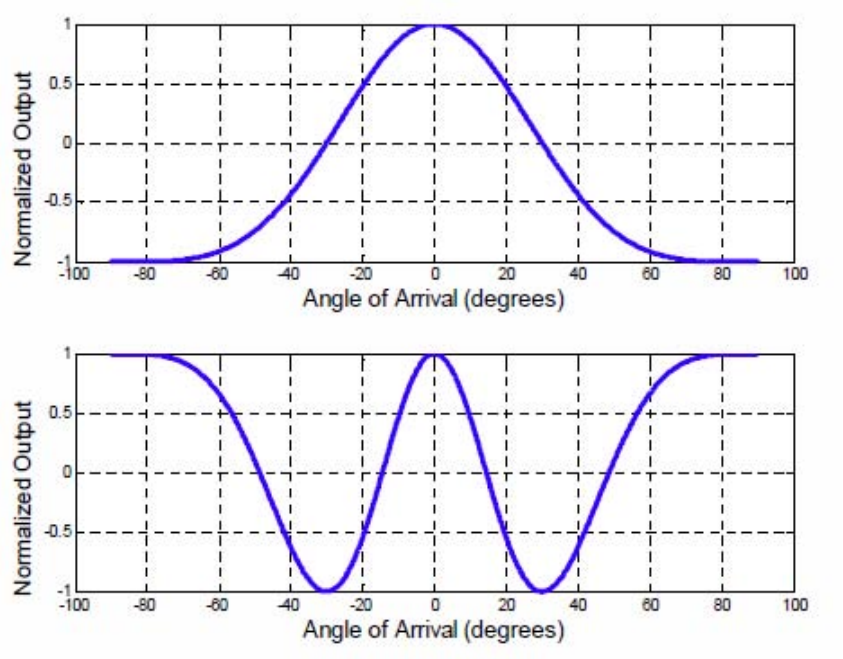

Figure 5. Output voltage vs AOA for $d = \frac{\lambda}{2}$ (top) and $d = \lambda$ (bottom) (From [2])

E. SUMMARY

This chapter gave a brief introduction to phase interferometry. It covered the basic equations used with respect to phase shifts. Quadrature demodulation was introduced, and equations for the voltage and phase differential between two elements presented. Ambiguity was also discussed and the AOA relationship to the folding waveform. The next chapter introduces the RSNS sequence and lays out two examples.

III. ROBUST SYMMETRICAL NUMBER SYSTEM

The idea behind applying the RSNS to DF is to reduce baselines and increase resolution [9]. This chapter reviews the basic concepts of RSNS theory and presents a design example.

A. ROBUST SYMMETRICAL NUMBER SYSTEM

An RSNS sequence is used to represent the symmetrical waveform out of antennas. The sequence is based on the following [10]:

$$\{x_m\} = [0,1,2,...,m-1,m,m-1,...,2,1] \tag{3.1}$$

where x_m is a row vector and $m > 0$ is an integer.

Each term is then repeated N times in an N-sequence RSNS [9]. The resultant form for one folding period is:

$$\{x_h\} = [0,0,...,0,1,1...,1,...,m-1,...,m-1,m,...m,m-1,...,m-1,...,1,...,1] \tag{3.2}$$

where h is an integer value $0 \le h < m$. The basic form of an RSNS sequence is given by the following:

$$\{x_h\} = \begin{cases} \left\lfloor \dfrac{h - s_i}{N} \right\rfloor, & s_i \le h \le Nm_i + s_i + 1 \\ \left\lfloor \dfrac{2Nm_i + N - h + s_i - 1}{N} \right\rfloor, & Nm_i + s_i + 2 \le h \le 2Nm_i + s_i - 1 \end{cases} \tag{3.3}$$

where s_i is the sequence shift value.

An N-channel RSNS is formed of vectors by picking N moduli m_i, and N shift values s_i, $1 \le i \le N$ [6].

An example is used to complete the explanation. An RSNS sequence is computed for the modulus set [3 4], where $m_1 = 3$ and $m_2 = 4$. Table 1 lays out the sequence.

I	0	1	2	3	4	5	6	7	8	9	10	11	12	13	14	15	16	17	18	19
$m_1 = 3$	0	1	1	2	2	3	3	2	2	1	1	0	0	1	1	2	2	3	3	2
$m_2 = 4$	0	0	1	1	2	2	3	3	4	4	3	3	2	2	1	1	0	0	1	1
n					**0**	**1**	**2**	**3**	**4**	**5**	**6**	**7**	**8**	**9**	**10**	**11**	**12**	**13**	**14**	

Table 1. RSNS sequence for $m_1 = 3$ and $m_2 = 4$ (From [11])

The sequence forms a set of unique vectors. The dynamic range of the sequence is defined as the number of unique vectors until a repeated vector occurs. For the given modulus set in Table 1 $\widehat{M} = 15$ (denoted by gray values of n). Dynamic range is an important quantity because for DF applications the $\widehat{M}$ gray values in Table 1 are mapped onto the field of view (FOV) of the antenna. Thus $\widehat{M}$ determines the DF resolution.

Dynamic range can be calculated in closed form for some cases.

- Case I: For $m_1 \geq 3$ and $m_2 = m_1 + 1$,

$$\widehat{M} = 3(m_1 + m_2) - 6 \tag{3.4}$$

- Case II: For $m_1 \geq 5$ and $m_2 = m_1 + 2$,

$$\widehat{M} = 3(m_1 + m_2) - 7 \tag{3.5}$$

- Case III: For $m_1 \geq 5$ and $m_2 = m_1 + C$, and $C \geq 3$,

$$\widehat{M} = 4m_1 + 2m_2 - 2 \tag{3.6}$$

The example from Table 1 demonstrates the dynamic range for two channels with relatively coprime moduli [8]. For Table 1, case I is the appropriate equation yielding $\widehat{M} = 3(3+4) - 6 = 15$.

When three channels are used, the closed form solutions for $\widehat{M}$ are given by the following two cases [8]:

- Case I: For $m_1 = 2^k - 1,\ m_2 = 2^k + 1$ for $m_1 \geq 3$,

$$\widehat{M} = \frac{3}{2} m_1^2 + \frac{15}{2} m_1 + 7 \tag{3.7}$$

- Case II: For $m_1 = 2m_2 + 1,\ m_3 = 4m_1 + 1$,

$$\widehat{M} = 6m_1^2 + 21m_1 + 3 \tag{3.8}$$

These closed form solutions only apply to the specific cases; for all other combinations, a dynamic range search algorithm is used [9].

B. RSNS INTERFEROMETER DESIGN

The following are the steps required to apply the RSNS to an interferometer DF system [2].

1. Select N, the number of channels required. Each channel is comprised of a pair of elements. All channels can share a reference element. Therefore the number of elements required is $N - 1$.

2. Identify an integer valued modulus for each channel $(m_1, m_2, ..., m_N)$, where the m_i are pairwise relatively prime.

3. Determine the system dynamic range based on the chosen moduli.

4. Define the number of folds within each modulus. The number of folds is calculated by dividing the dynamic range by the period of each modulus

$$n_i = \frac{\widehat{M}}{2Nm_i} \qquad i = 1, 2, ..., N\ . \tag{3.9}$$

5. Determine the required antenna spacing for each channel

$$d_i = n_i \frac{\lambda}{2}. \tag{3.10}$$

6. Re-map the FOV. This is sometimes desired as wide angle data is generally degraded. To re-map the FOV, a scaling factor, ξ, is created which effectively enhances resolution and decreases antenna spacing [2]. The maximum FOV equation is equated to the scaled FOV equation yielding:

$$d\sin(\theta) = d'\sin(\theta') \tag{3.11}$$

where the primed quantities are associated with the scaled antenna. Equation (3.11) then rearranges to define the scaling factor as:

$$\xi = \frac{d'}{d} = \frac{\sin(\theta)}{\sin(\theta')} \tag{3.12}$$

7. Determine the folding waveform thresholds. The thresholds are calculated using a MATLAB script, based on the equation:

$$V_{j,m_i} = \cos\left(\frac{m_i - j + \frac{1}{2}}{m_i}\pi\right), \qquad 1 \le j \le m_i \tag{3.13}$$

8. Calculate the phase adjustment term for each channel, ς_i. The phase adjustment properly aligns the folding waves and introduces the shift values, s_i, for each channel is incorporated into Equation (2.4)

$$V_{out}(\theta) = \cos(kd\sin\theta + \varsigma) \tag{3.14}$$

C. SINGLE CHANNEL THEORY

The idea behind the single channel in RSNS is that the data from one channel can be used to simulate as many channels as desired. The single channel theory described here is defined in [12]. One unambiguous fold of one channel is all that is needed to generate a waveform with an arbitrary number of folds in the processor. For RSNS processing the virtual spacing for channel i is

$$d_{v_i} = C_i d \tag{3.15}$$

where C_i is the scale factor for the waveform and d is the physical element spacing for the single channel.

The voltage for the AOA can be found for any spacing d_{v_i} as long as the output voltage from the physical spacing gives a single fold or less. The amplitude folding waveform is

$$V_i(\theta) = \cos\left(\frac{C_i kd}{2}\sin\theta\right) = \cos\left(\frac{kd_{v_i}}{2}\sin\theta\right) = \cos\left(\frac{C_i \triangle\phi}{2}\right). \tag{3.16}$$

The unambiguous single fold is possible if the physical spacing $d < 1\lambda$.

When the number of channels and the moduli are chosen, the number of folds and virtual spacings are computed. The RSNS processing then uses the virtual waveform voltages from Equation (3.16).

If the single channel theory is used for a four channel system $[m_1, m_2, m_3, m_4]$, the virtual spacings are $d_{v_i}, i = 1,2,3,4$. The scale factor in this case is found by rearranging Equation (3.15) to $C_i = d_{v_i}/d$. As with the traditional RSNS, the I and Q data are used to compute the phase difference $\triangle\phi$. Equation (3.16) is used to find the virtual folding waveform voltages

$$V_i = \cos\left(\frac{C_i \triangle\phi}{2} + \varsigma_i\right) \tag{3.17}$$

where ς_i is the phase shift to center the dynamic range to broadside. The V_i values are used to assign the phase difference to the appropriate RSNS bin resulting in the estimated AOA.

D. EXAMPLE

This example follows the eight steps listed in the previous section and steps through each decision and calculation.

1. A 2 channel design is selected so $N = 2$.

2. The moduli are chosen to be pairwise relatively prime and are $m_1 = 5$ and $m_2 = 9$.

3. The MATLAB dynamic range search script was used to obtain $\widehat{M} = 36$, or from Equation (3.6) $\widehat{M} = 4(5) + 2(9) - 2 = 36$.

4. The number of folds were calculated to be:

$$n_1 = \frac{\widehat{M}}{2Nm_1} = \frac{36}{(2)(2)(5)} = 1.8$$

$$n_2 = \frac{\widehat{M}}{2Nm_2} = \frac{36}{(2)(2)(9)} = 1$$

5. The antenna spacing was determined for a frequency of 2.4 GHz, which yields a wavelength, λ, of 12.5 cm:

$$d_1 = n_1 \frac{\lambda}{2} = 1.8 \frac{12.5}{2} = 11.25 \text{ cm}$$

$$d_2 = n_2 \frac{\lambda}{2} = 1 \frac{12.5}{2} = 6.25 \text{ cm}$$

6. This example does not change the FOV, so $\xi = 1$. Thus the DF is measured over the range $-90^\circ \le \theta \le 90^\circ$.

7. The threshold values were calculated in a MATLAB script according to Equation (3.13) and are given below in Table 2.

$m \setminus j$	0	1	2	3	4	5	6	7	8
5	-0.9511	-0.5878	0	0.5878	0.9511	0	0	0	0
9	-0.9848	-0.8660	-0.6428	-0.3420	0	0.3420	0.6428	0.8660	0.9848

Table 2. Threshold values $V_{j,m}$ for $\widehat{M} = 36$,

8. The phase adjustments were also calculated with a MATLAB script according to Equation (3.14) and are given below in Table 3.

Channel 1, ς_1	-1.2566 radians
Channel 2, ς_2	-1.5708 radians

Table 3. Phase Adjustments for $\widehat{M} = 36$

The transfer function plot of estimated AOA versus true AOA is shown in Figure 6. If the two values were exactly equal a diagonal line would bisect the plot. The presence of the stair stepping is visible due to the quantization bin width in the RSNS code. There are no ambiguities, which means that for a given value of real AOA there is only one value for estimated AOA that is returned from the RSNS.

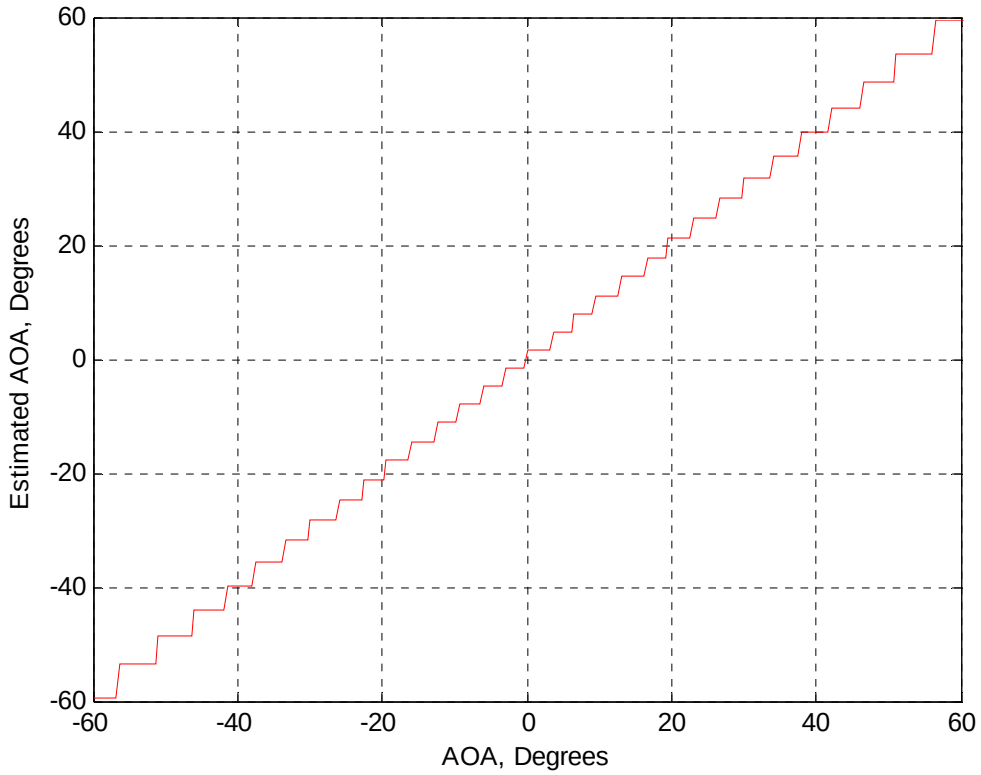

Figure 6. Ideal Transfer Function for Moduli set [5 9]

If there is thermal noise or phase errors in the channel then the transfer function is degraded. For example, when an error of 36° is introduced into the channels the estimated AOA values no longer follow the center diagonal, but shift up to the left of the diagonal as seen in Figure 7. The dashed line represents a perfect estimated AOA with given AOA, while the solid line is the simulated data with error.

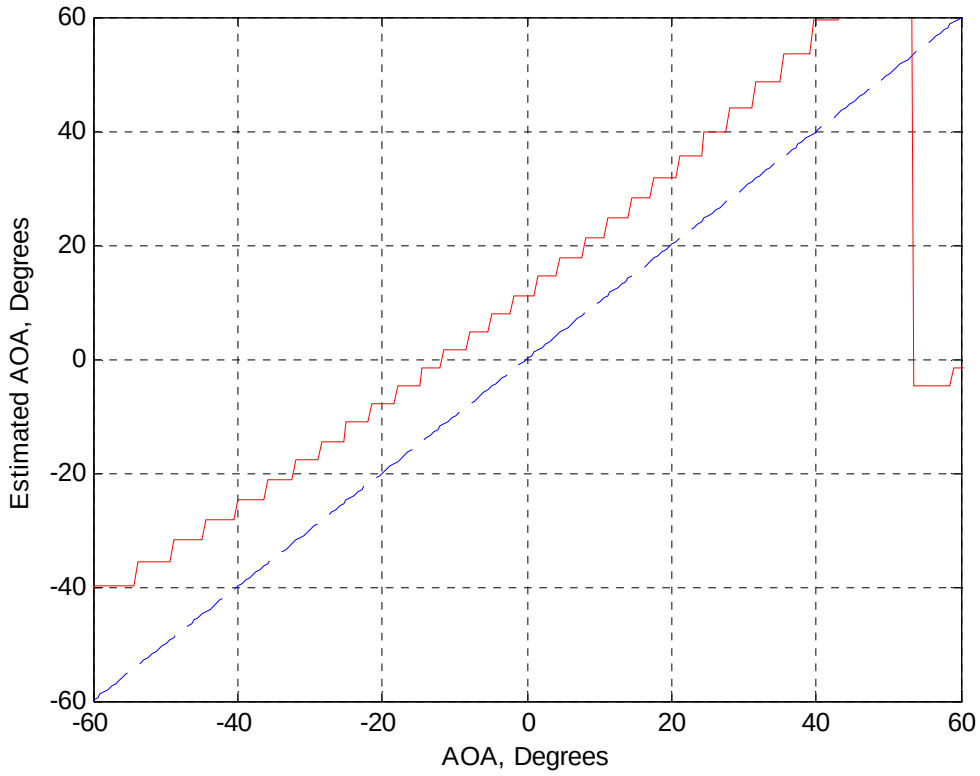

Figure 7. Transfer Function for Moduli set [5 9] with 36° of channel error

E. SUMMARY

This chapter introduced RSNS theory as well as single channel theory. Interferometer design guidelines and examples were given. The next chapter discusses the simulations completed in MATLAB to assess the effects of noise and the results that were obtained.

IV. COMPUTER SIMULATION AND RESULTS

This chapter provides the explanation of the MATLAB code that was used and the results from various simulation runs using multiple sets of moduli and numbers of channels.

A. MATLAB SIMULATION

A study of two, three, and four channel moduli sets was completed. The objective was to determine how the RSNS AOA estimates were affected by the SNR values. More specifically, is there an advantage to using more channels for a given resolution $\widehat{M}$? The MATLAB code is a modified version of one that was created and appended from several past research projects. Figure 8 lays out the contents of the code in a flow diagram. The bold boxes represent the MATLAB script files and the plain boxes represent the variables or calculations accomplished. The **Virtual_datafile_generator.m** was run first for a given number of moduli and their values. It calculated the threshold values and called on the script **findDynamicRange.m** to calculate the dynamic range, $\widehat{M}$. The **Virtualnoisejb.m** file was then run to simulate a plane wave incident over a range of angles. It uses the previously calculated data and the incidence angles to calculate I and Q. From the I and Q values, the estimated AOA was obtained. Noise was added in the process to observe its effect on the AOA estimates.

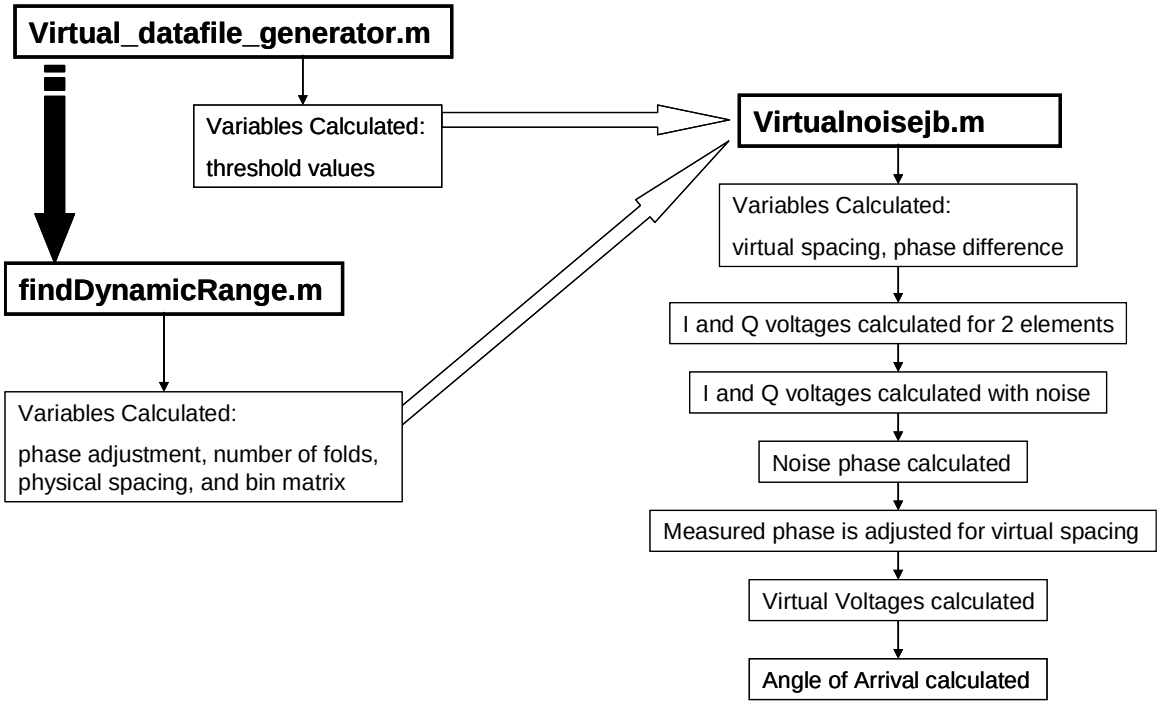

Figure 8. MATLAB code flow diagram

The AOA was calculated for 5 SNRs over a range of angles from $-90^{\circ} \le \theta \le 90^{\circ}$. The root mean square (RMS) error values and standard deviations were calculated for each angle at each SNR. Each angle was run 25 times at each SNR. As stated in Chapter I, using angles near $\pm 90^{\circ}$ is not reasonable for the antenna, so the reporting is limited to a more realistic range of $\pm 60^{\circ}$.

B. SMALL DYNAMIC RANGE

The first sets of moduli simulated were chosen to give a small dynamic range. The moduli sets are shown below in Table 4. The angular resolution at broadside was also calculated to give a reference value for the errors out of the simulation.

Number of Channels	2 Channel	3 Channel	4 Channel
Dynamic Range	102	104	117
Moduli	[11 30]	[5 7 9]	[3 4 5 7]
Broadside Angular Resolution (degrees)	1.76	1.73	1.54

Table 4. Small Dynamic Range Moduli

The purpose of the first three sets of moduli was to compare the performance of a small dynamic range using 2, 3, and 4 channels. A higher error is expected for the lower SNR values so those have been plotted together giving SNRs of 10 dB, 15 dB, 20 dB, 25 dB, and 30 dB all on one plot.

Figures 9, 10, and 11 show the trends in RMS error for the low SNR values. Each set shows an apparent periodic behavior in the data versus AOA. In Figure 9, the data for 2 channels peaks twice around 0° while showing lower error values in regions near $\pm 35^\circ$. Due to the overall high error values, this moduli set at these SNRs is of no use. Errors that are $\geq 5^\circ$ are not tolerable, and hence SNRs below 20 dB are not acceptable.

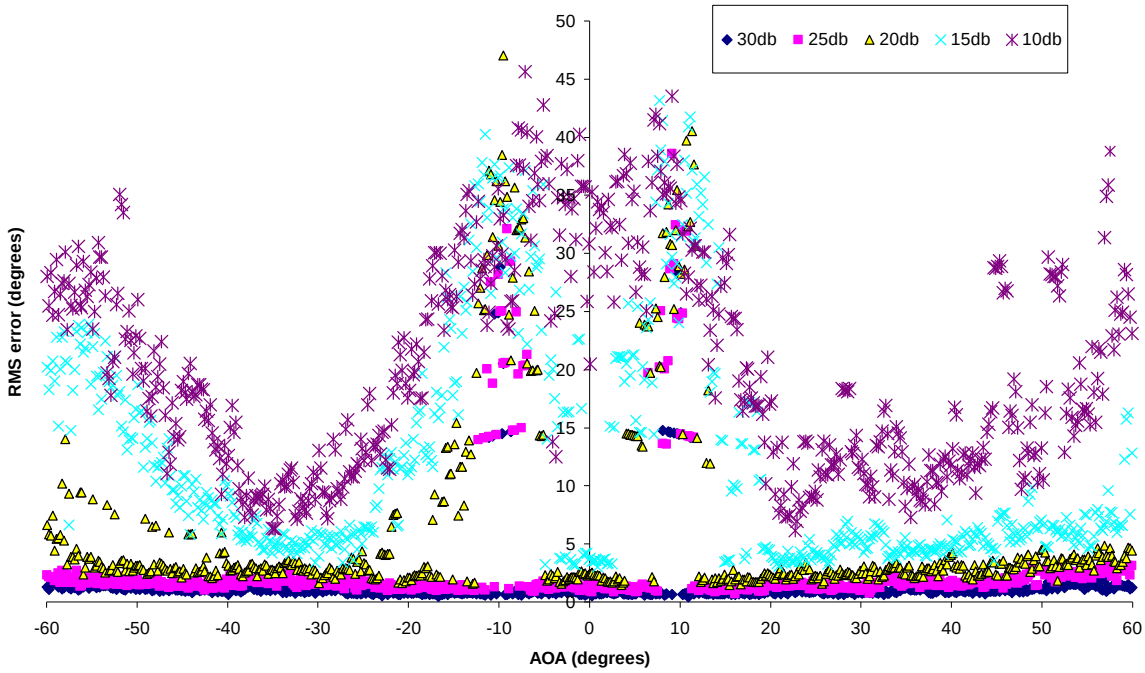

Figure 9. RMS error for 2 channels, $\widehat{M} = 102$, and SNRs from 10 dB to 30 dB

In Figure 10, the data for 3 channels also shows a periodic nature, however, there are five peaks distributed throughout the AOA range. This 3 channel moduli set yields poor results when compared with the set in Figure 9. In this case large errors occur for SNRs below 30 dB.

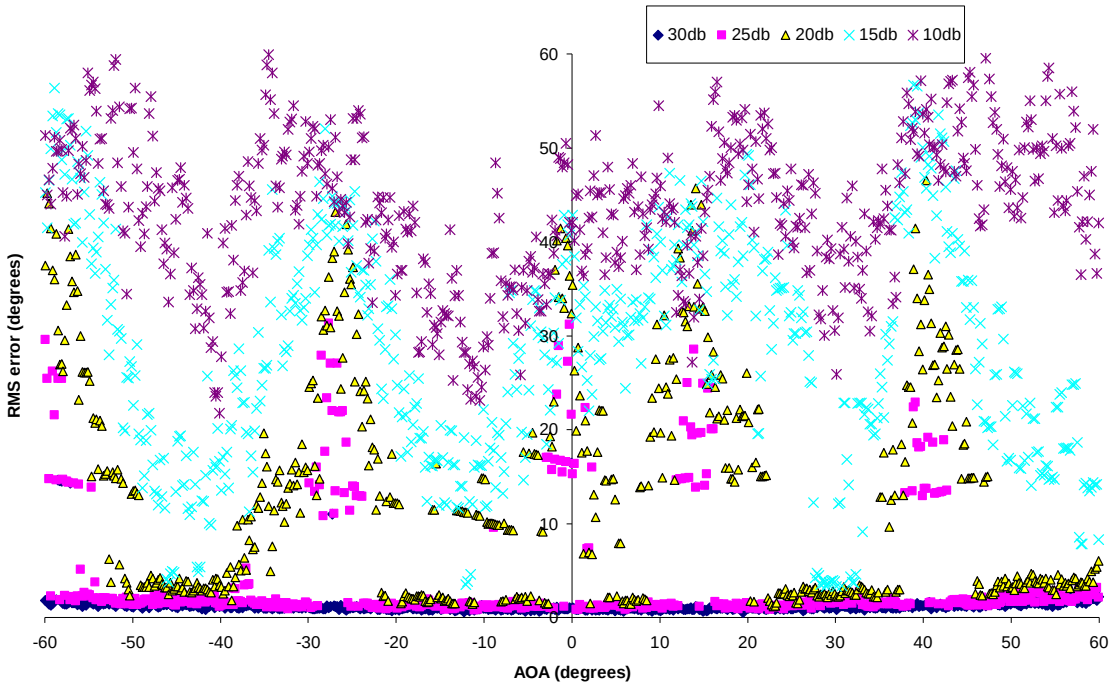

Figure 10. RMS error for 3 channels, $\widehat{M} = 104$, and SNRs from 10 dB to 30 dB

In Figure 11, the data for 4 channels shows the periodicity as seen in Figures 9 and 10, however the peaks are more difficult to distinguish. This 4 channel data yields slightly better error results than the 3 channel, especially in the range from $\pm 15^{\circ}$. Again, it appears that 30 dB or greater SNR is required to keep the RMS error below 5°.

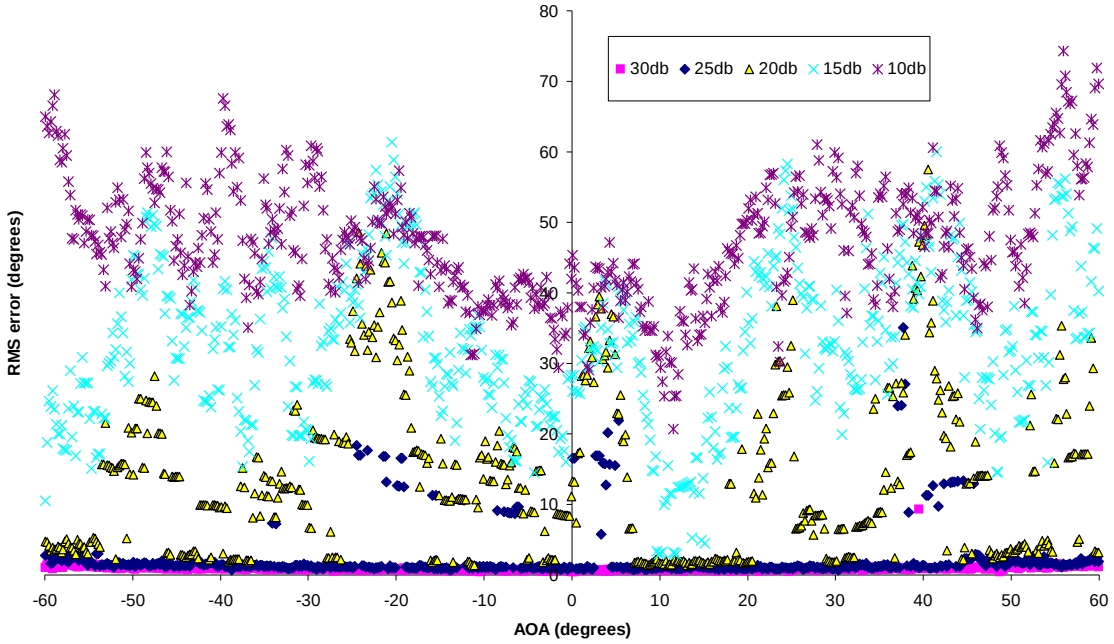

Figure 11. RMS error for 4 channel, $\widehat{M} = 117$, and SNRs from 10 dB to 30 dB

As the SNR is increased, the resulting AOA estimations are expected to improve. Figures 12, 13, and 14 show the RMS error trends with respect to 35 dB, 40 dB, 45 dB, and 50 dB. In Figure 12 there is an outlier point at 9°, for an SNR of 35 dB, with a value of 20.6°. For the purposes of this plot, that point is removed. In the remaining data, the maximum error is 1.53° which is below the broadside angular resolution of the moduli set.

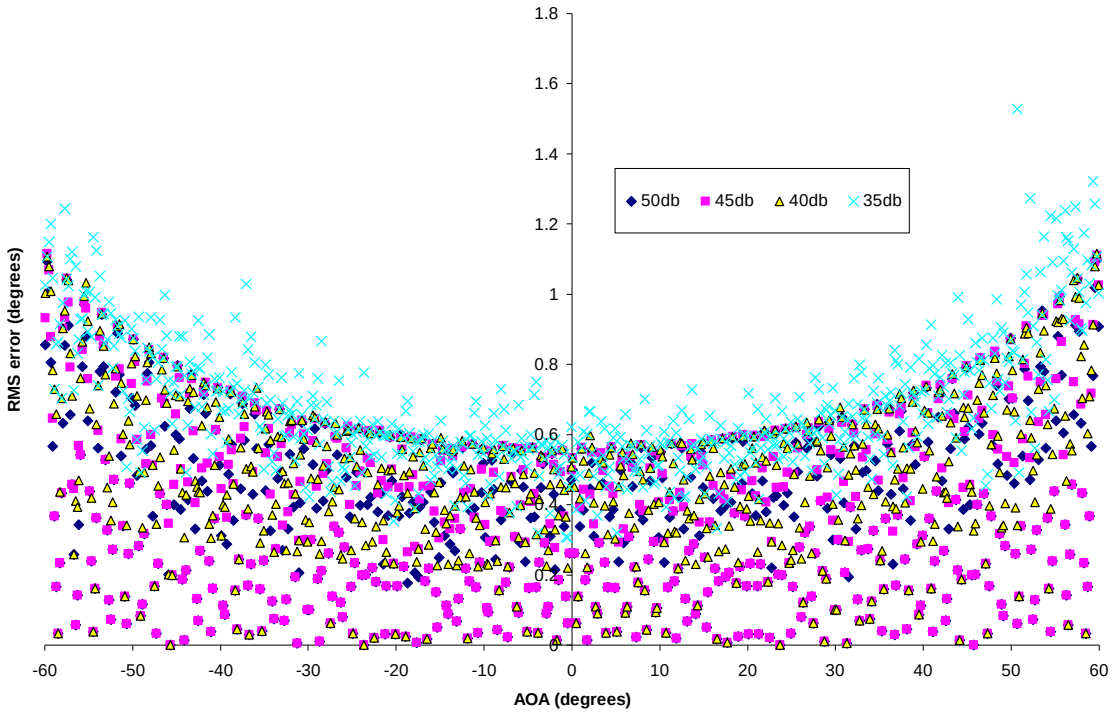

Figure 12. RMS error for 2 channels, $\widehat{M} = 102$, and SNRs from 35 dB to 50 dB

In Figure 13, there is a bounded distribution of the RMS error points. The highest error value is 1.98° and the broadside angular resolution for this set of moduli is 1.73°. The trend of the error shows an increase as the AOA approaches $\pm 60^{\circ}$. This behavior is expected due to the increase in bin size with angle. When noise causes an estimate to move to the adjacent bin, the error in degrees is larger for bins farther from broadside.

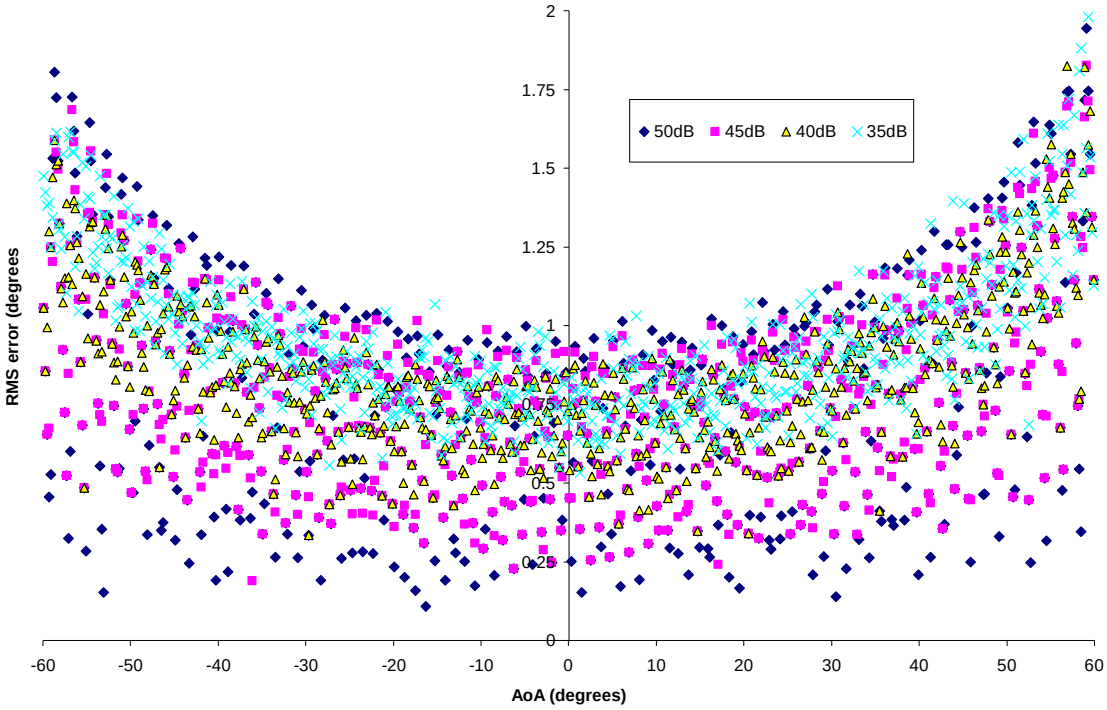

Figure 13. RMS error for 3 channels, $\widehat{M} = 104$, and SNRs from 35 dB to 50 dB

The behavior of the data in Figure 14 is very similar to that of Figure 13. The highest error value on this plot is 1.19° which is well within the 1.54° broadside angular resolution.

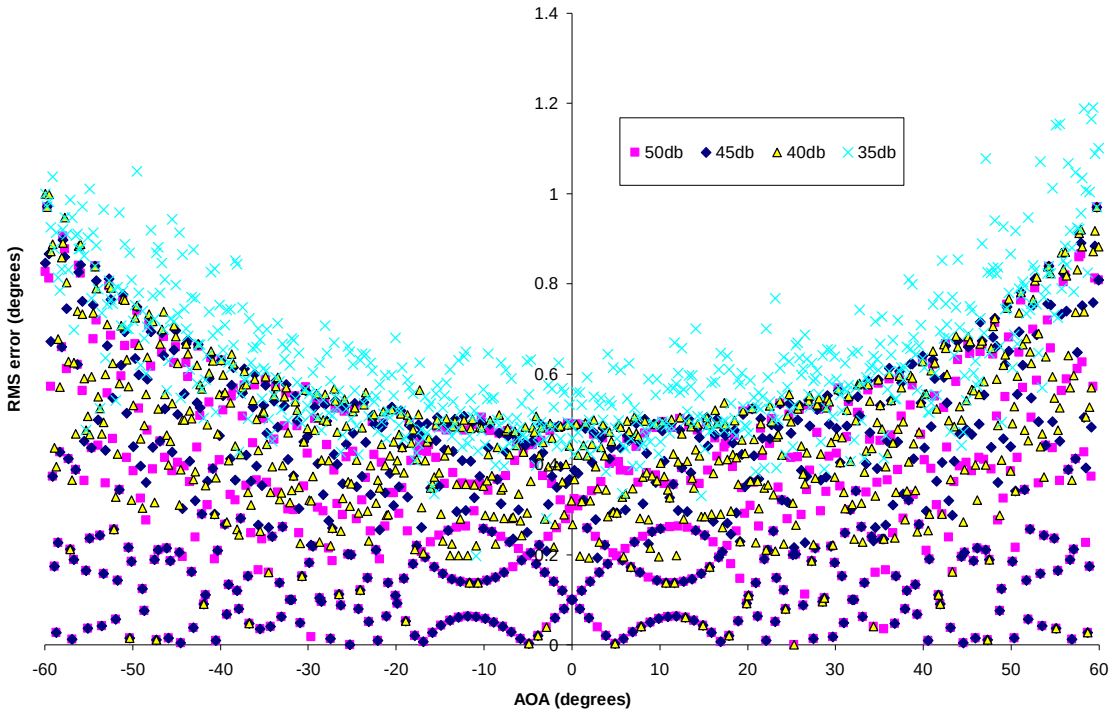

Figure 14. RMS error for 4 channels, $\widehat{M} = 117$, and SNRs from 35 dB to 50 dB

In these simulations, the difference between the number of channels is seen. While at the higher SNR values, the error is better for the higher channel moduli sets, the 2 channel moduli set performed better than the 3 channel for the low SNR values.

C. LARGE DYNAMIC RANGE

The second sets of moduli simulated were chosen to give a large dynamic range. The moduli sets are shown below in Table 5.

Number of Channels	2 Channel	3 Channel	4 Channel
Dynamic Range	399	396	410
Moduli	[67 68]	[9 14 17]	[5 6 7 13]
Broadside Angular Resolution (degrees)	0.45	0.45	0.44

Table 5. Large Dynamic Range Moduli

As with the small dynamic ranges, the large dynamic range moduli were run to compare the performance using 2, 3, and 4 channels. Figures 15, 16, and 17 depict the lower SNR values. These plots look distinctively different than the small dynamic range plots.

In Figure 15, for $\widehat{M} = 399$, there is a different trend within the 30 dB SNR. The error values are distinctively lower in the $\pm 5^{\circ}$ range, however the 30 dB SNR is the only one to show a low linear error trend just to the left of 0°. The values of all of these errors were above the acceptable value.

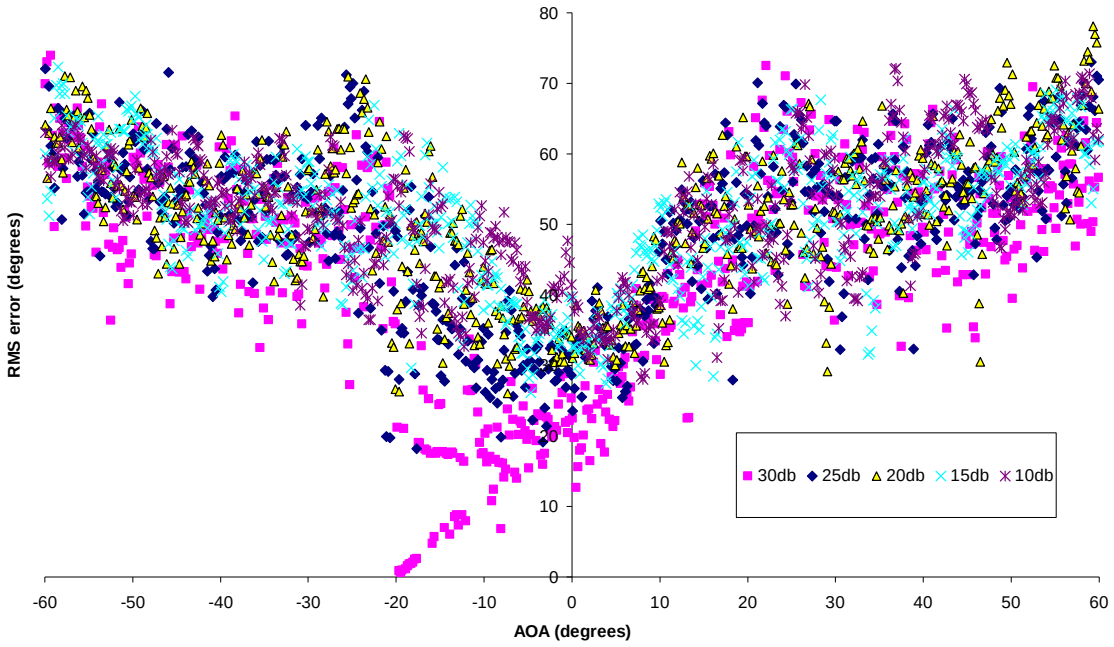

Figure 15. RMS error for 2 channels, $\widehat{M} = 399$, and SNRs from 10 dB to 30 dB

Figure 16 shows the RMS error values for 3 channels, $\widehat{M} = 396$. This 3 channel set of moduli shows similar errors to that of Figure 15. There is a periodic shape to the data similar to that found in the small dynamic range data, but the error values are still too high to be usable.

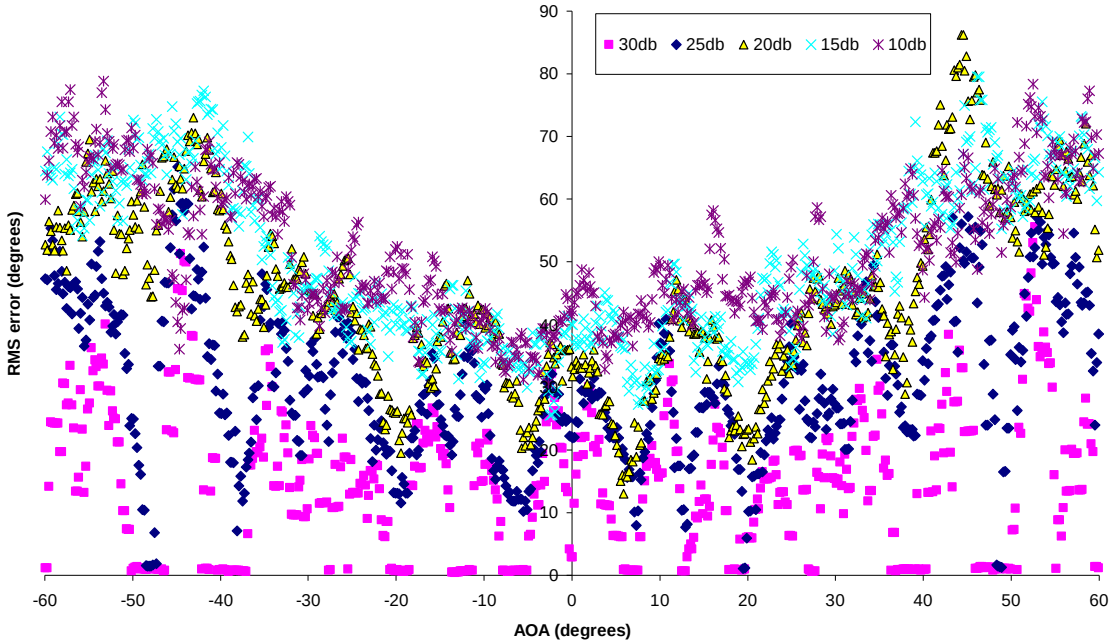

Figure 16. RMS error for 3 channels, $\widehat{M} = 396$, and SNRs from 10 dB to 30 dB

Figure 17 shows the error data for 4 channels, $\widehat{M} = 410$. The periodic nature of this data is more difficult to see, but it is still present. This data has an improved error in the range of $\pm 45^{\circ}$ but is still too high to be usable.

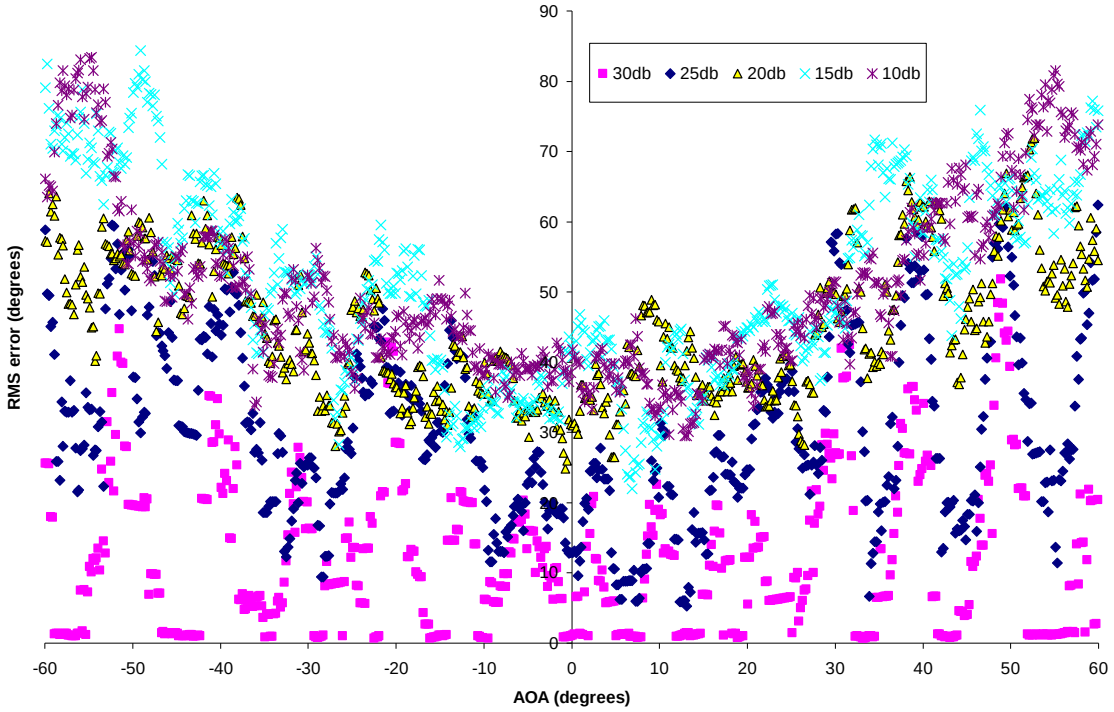

Figure 17. RMS error for 4 channels, $\widehat{M} = 410$, and SNRs from 10 dB to 30 dB

Figures 18, 20, and 22 show the higher end of the SNR values. Figure 18 shows the error for 2 channels, $\widehat{M} = 399$. This data is showing the same error trend that was seen in Figure 15 for the 30 dB SNR values. There is a large reduction in error for $\pm 20^{\circ}$, however the error values outside of this are still very high.

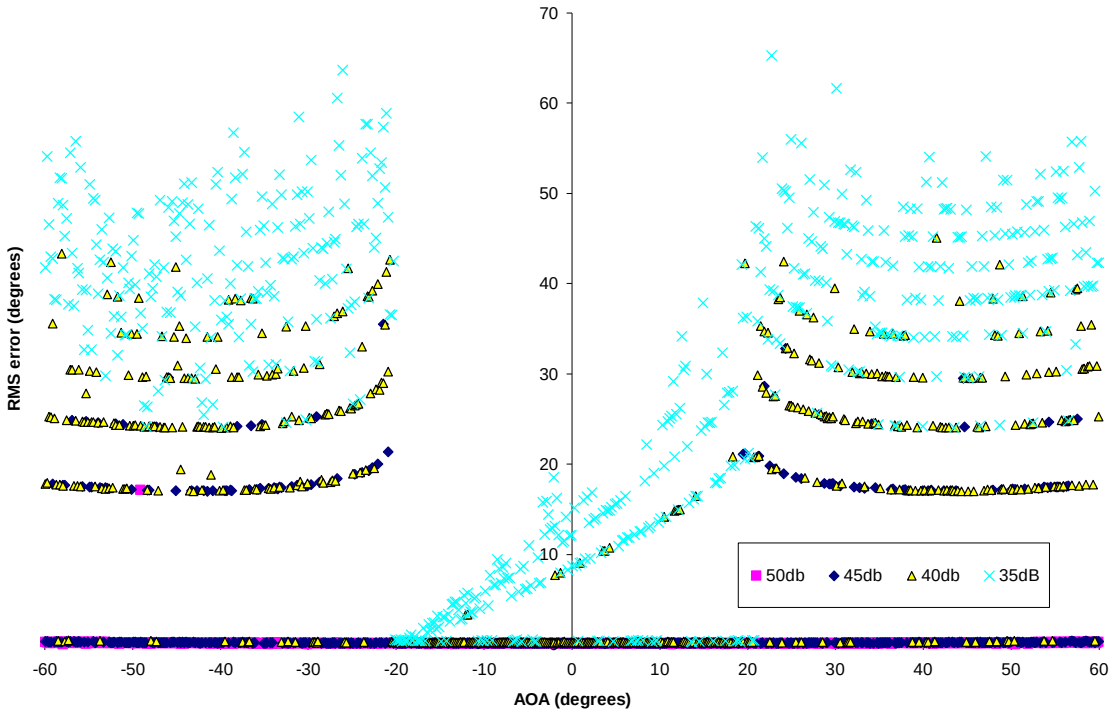

Figure 18. RMS error for 2 channels, $\widehat{M} = 399$, and SNRs from 35 dB to 50 dB

To have a better understanding of the data, a linear log plot was produced for the data in Figure 18. Figure 19 shows that much of the data still falls within the broadside angular resolution of 0.45°. On the log plot this equates to a value of -0.35. Many of the SNR results are unusable, but the data for 50 dB are very good.

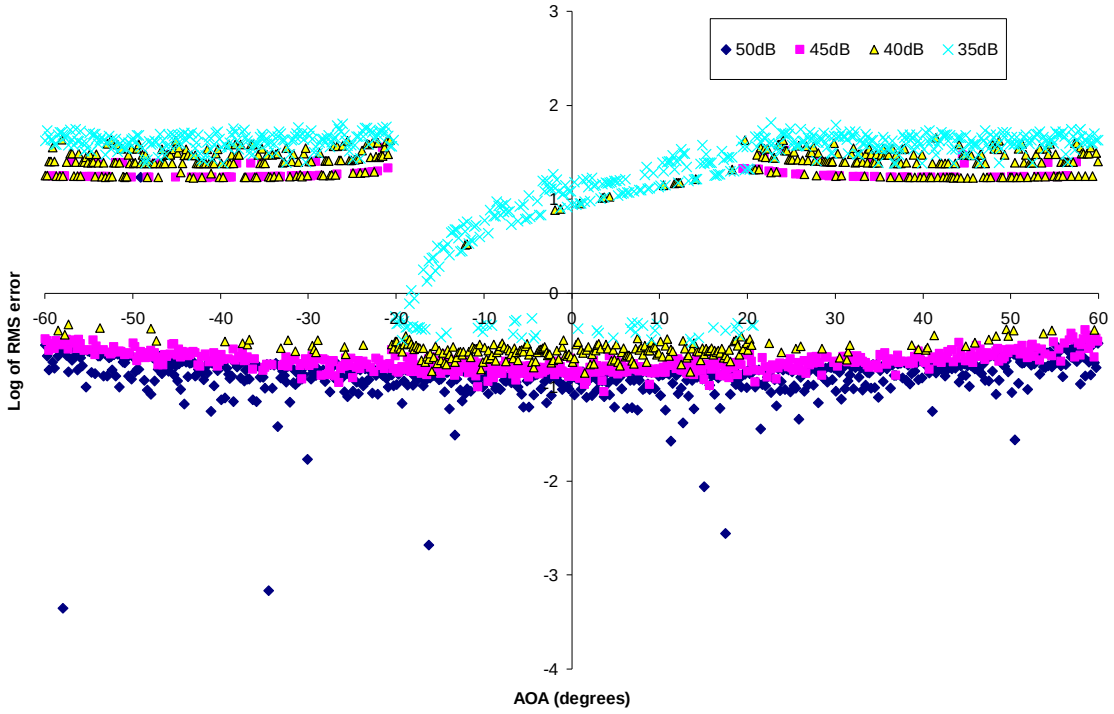

Figure 19. 2 channel Log(RMS error), $\widehat{M} = 399$, and SNRs from 35 dB to 50 dB

Figure 20.

Figure 20 shows the error values for 3 channels, $\widehat{M} = 396$. While this data does not have the same error drop off as in Figure 18, the overall error values are much decreased. The error values for SNRs of 35 dB and 40 dB are still much above the usable range, however the error for 45 dB and 50 dB are favorable.

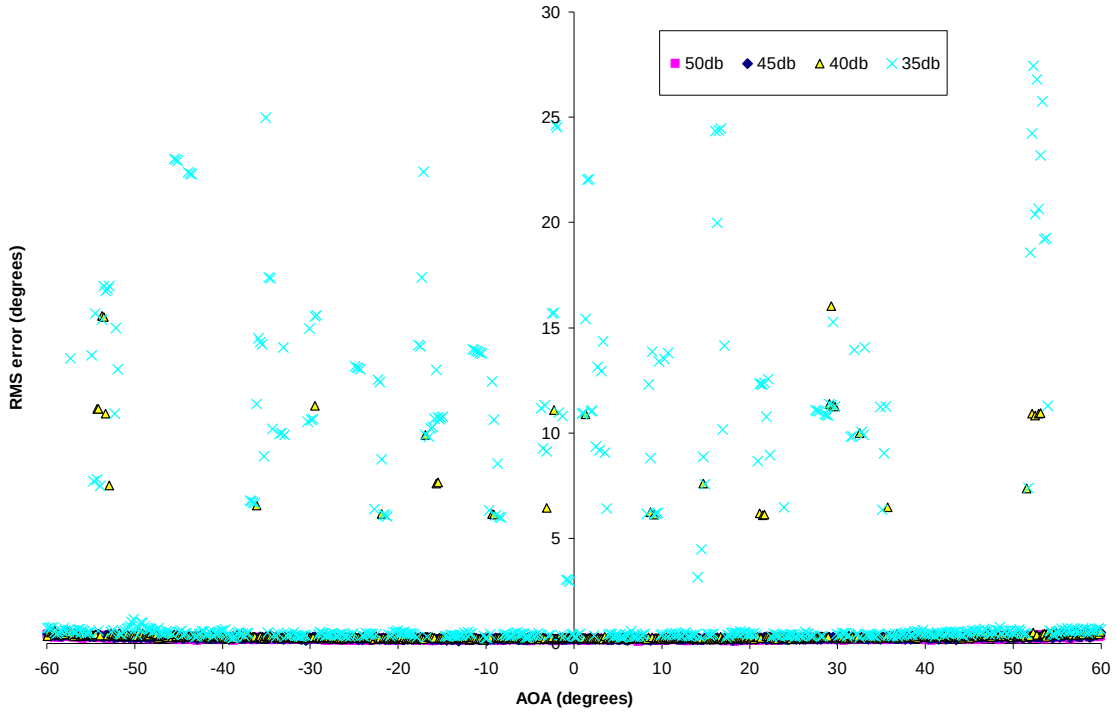

Figure 21. RMS error for 3 channels, $\widehat{M} = 396$, and SNRs from 35 dB to 50 dB

A linear log plot was produced for the data in Figure 20. Figure 21 shows that much of the data falls within the broadside angular resolution of 0.45° even more than for Figure 19. On the log plot this equates to a value of -0.35. Only a few of the SNR results are unusable. Data for 45 dB and 50 dB are very good.

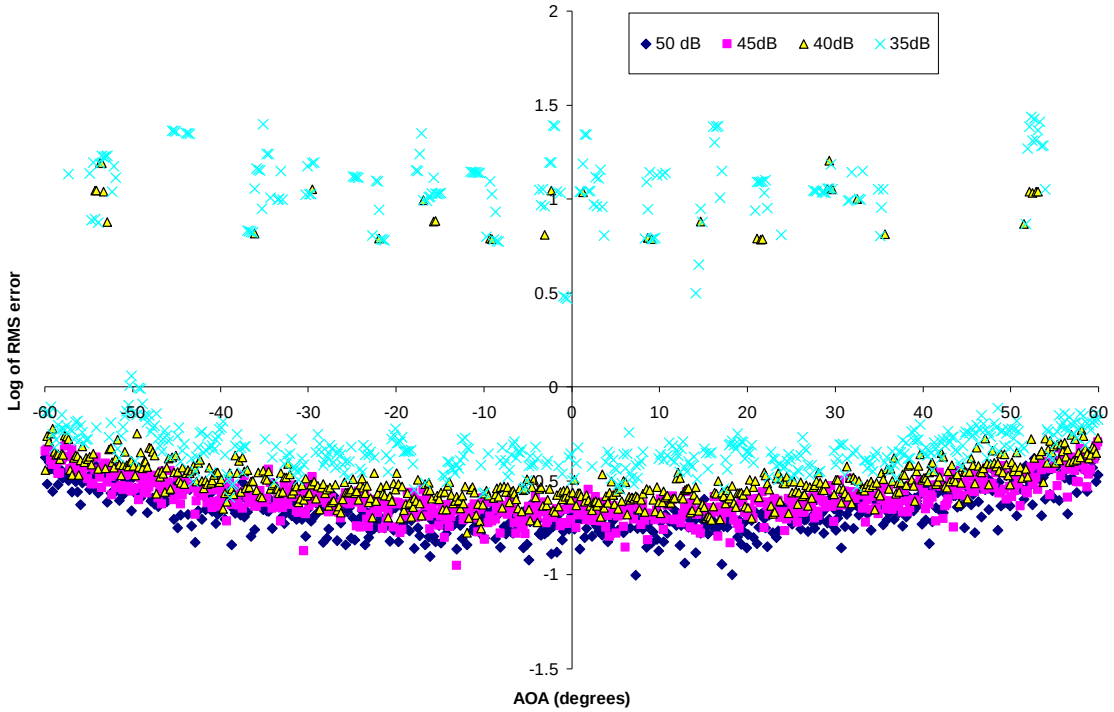

Figure 22. 3 channel Log(RMS error), $\widehat{M} = 396$, and SNRs from 35 dB to 50 dB

Figure 22 shows the error values for 4 channels, $\widehat{M} = 410$. This error data shows even better results than in Figure 20. The overall error is decreased and there is a noticeable decrease in error around $\pm 40^{\circ}$. SNRs of 40 dB to 50 dB have low enough error values to be usable, but the high error in the 35 dB data makes it unusable.

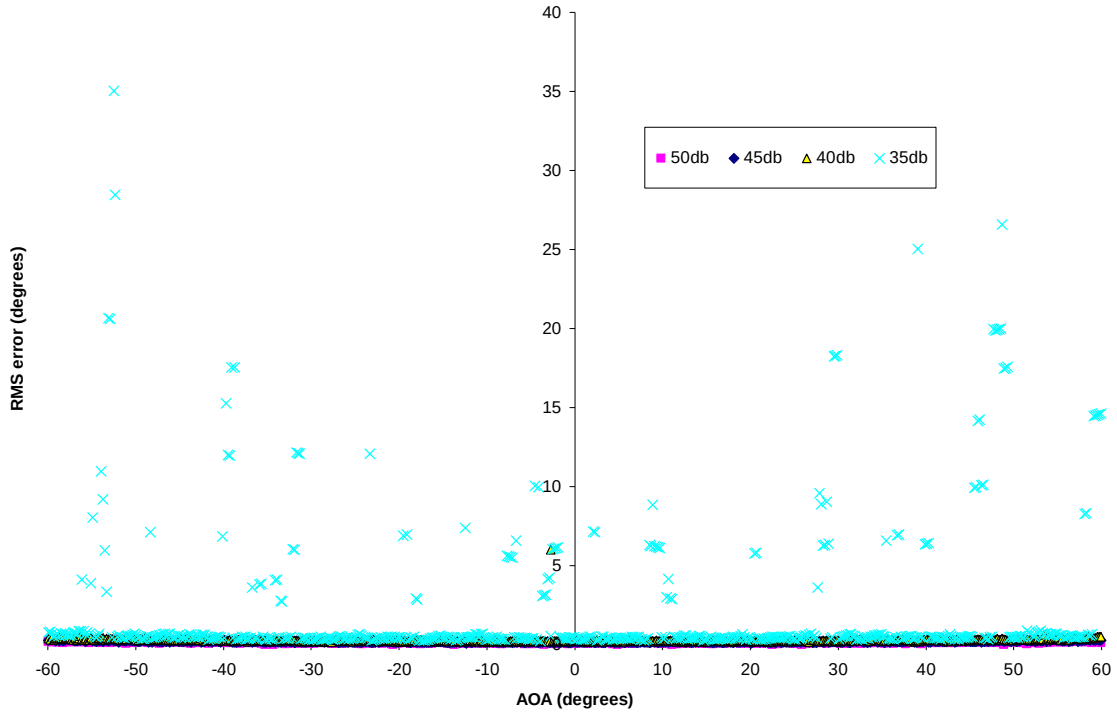

Figure 23. RMS error for 4 channels, $\widehat{M} = 410$, and SNRs from 35 dB to 50 dB

A linear log plot was produced for the data in Figure 22. Figure 23 shows that like Figure 21, much of the data falls within the broadside angular resolution of 0.44°, even more than for Figure 21. On the log plot this equates to a value of -0.36. Only one of the SNR results are unusable while data for 40 dB to 50 dB are very good.

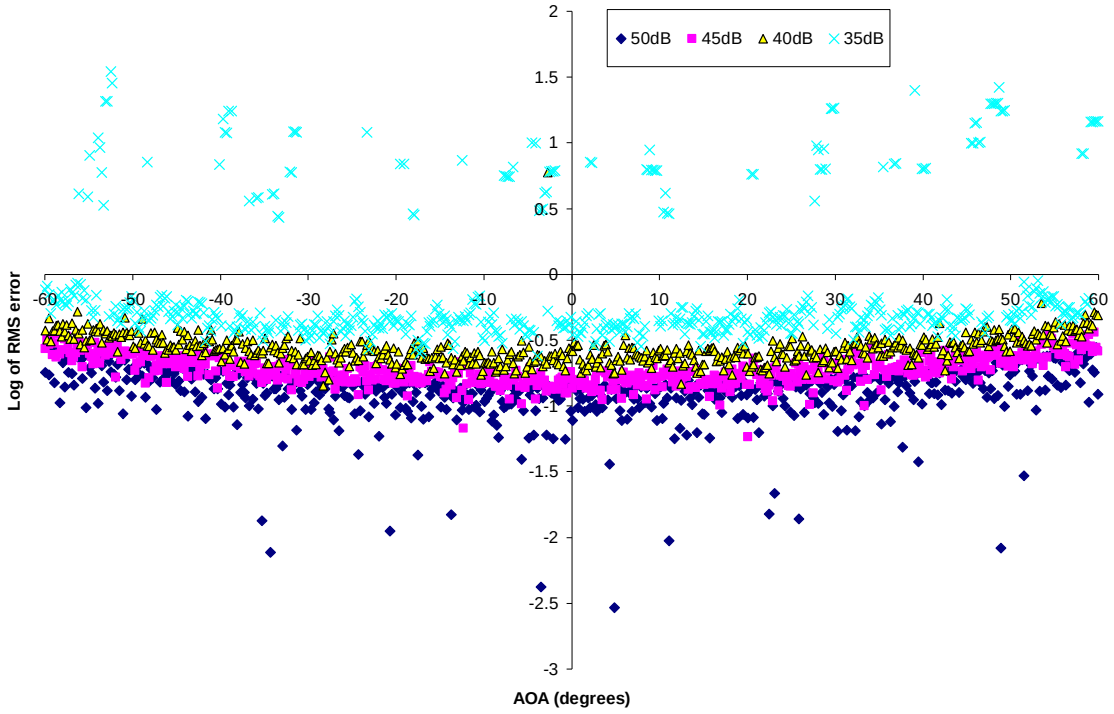

Figure 24. 4 channel Log(RMS error), $\widehat{M} = 410$, and SNRs from 35 dB to 50 dB

In these simulations, the difference between the number of channels is also seen. Unlike the small dynamic range moduli, at every SNR except 50 dB the 2 channel error data did not perform as well. The best error results were shown with the 3 and 4 channel data. The 4 channel data performed slightly better than the 3 channel, but overall the two sets were very similar.

D. THREE CHANNEL COMPARISON

The third sets of moduli simulated were chosen to give a small, medium, and large dynamic range using only a 3 channel setup. The moduli sets are shown below in Table 6.

Dynamic Range	85	276	426
Moduli	[3 5 11]	[9 11 19]	[13 15 19]
Broadside Angular Resolution (degrees)	2.11	0.65	0.42

Table 6. Moduli for a 3 Channel Comparison

The purpose of the comparison was to examine the error values for three different dynamic ranges for 3 channels. Figures 24, 25, and 26 show the trends in RMS error for low SNR.

In Figure 24, the data for low resolution shows a dip in error values around $\pm 25^{\circ}$ for low SNRs while showing increased values as AOA approaches $\pm 60^{\circ}$. The error values from 25 dB to 30 dB are below the 5° threshold, and therefore these results are very favorable.

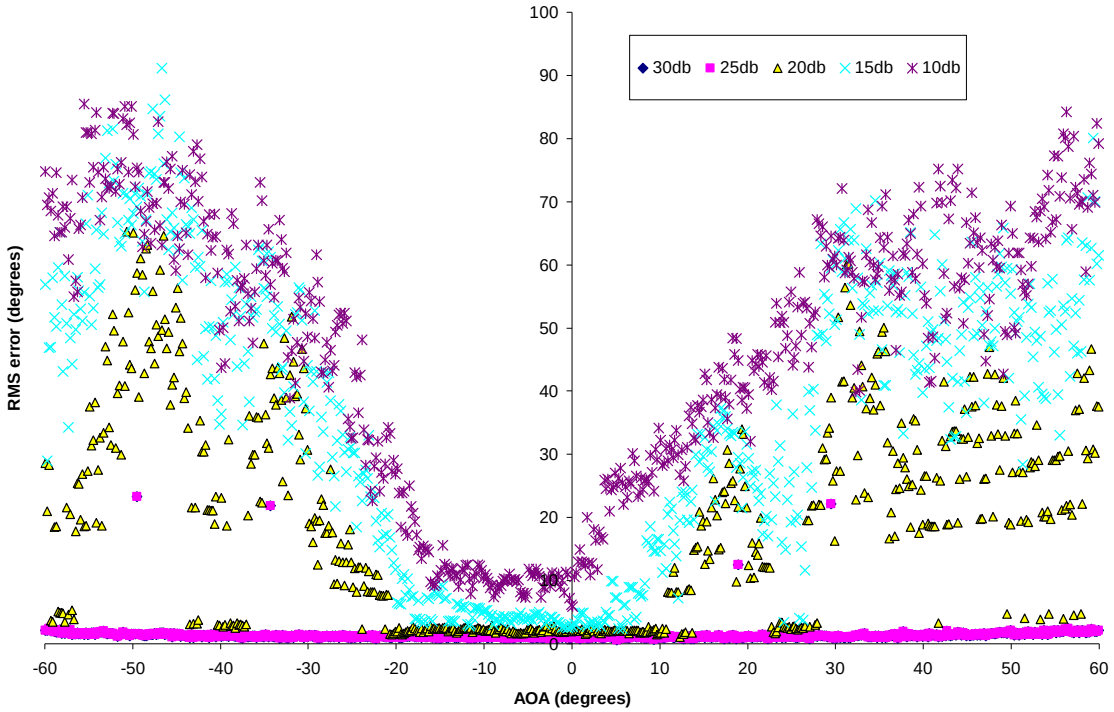

Figure 25. RMS error for 3 channels, $\widehat{M} = 85$, and SNRs from 10 dB to 30 dB

Figure 25 shows the error values for 3 channels, $\widehat{M} = 276$. This error data shows the periodic behavior as seen in some of the previous figures. While this data does not show the same low error as in Figure 24, the error is more constant around $\pm 40^{\circ}$ but still completely out of the usable range of values.

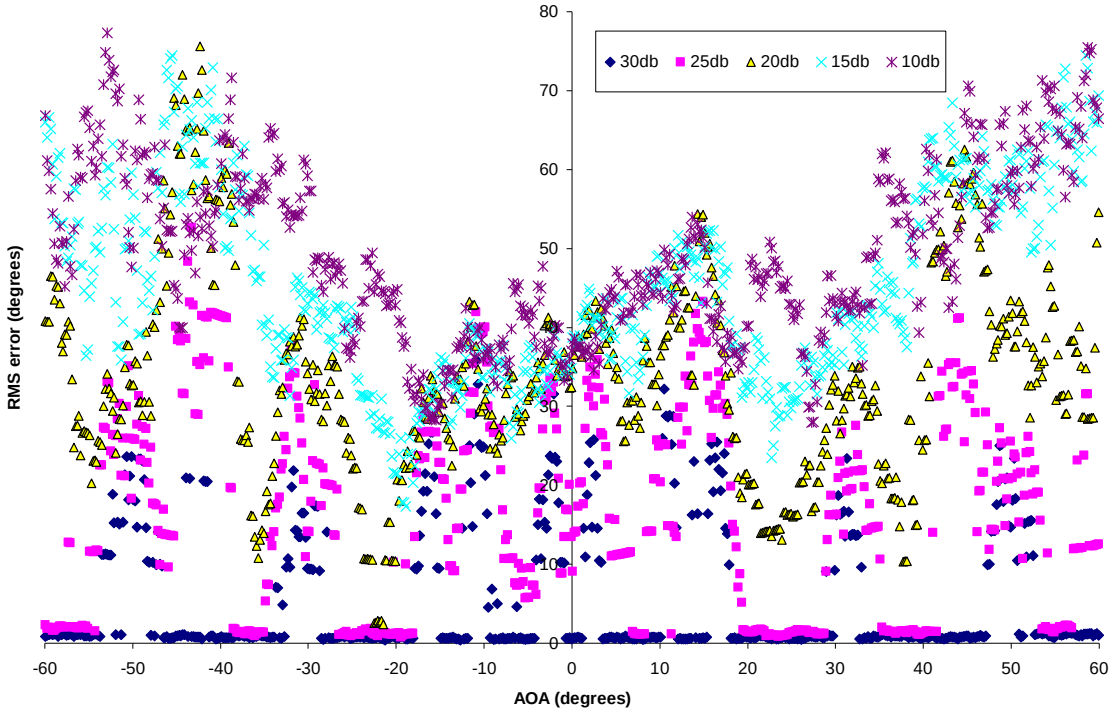

Figure 26. RMS error for 3 channels, $\widehat{M} = 276$, and SNRs from 10 dB to 30 dB

Figure 26 shows the error for 3 channels, $\widehat{M} = 426$. This figure has the same periodic behavior as Figure 25, but the overall error response is actually worse than for the previous dynamic range moduli and thus not usable.

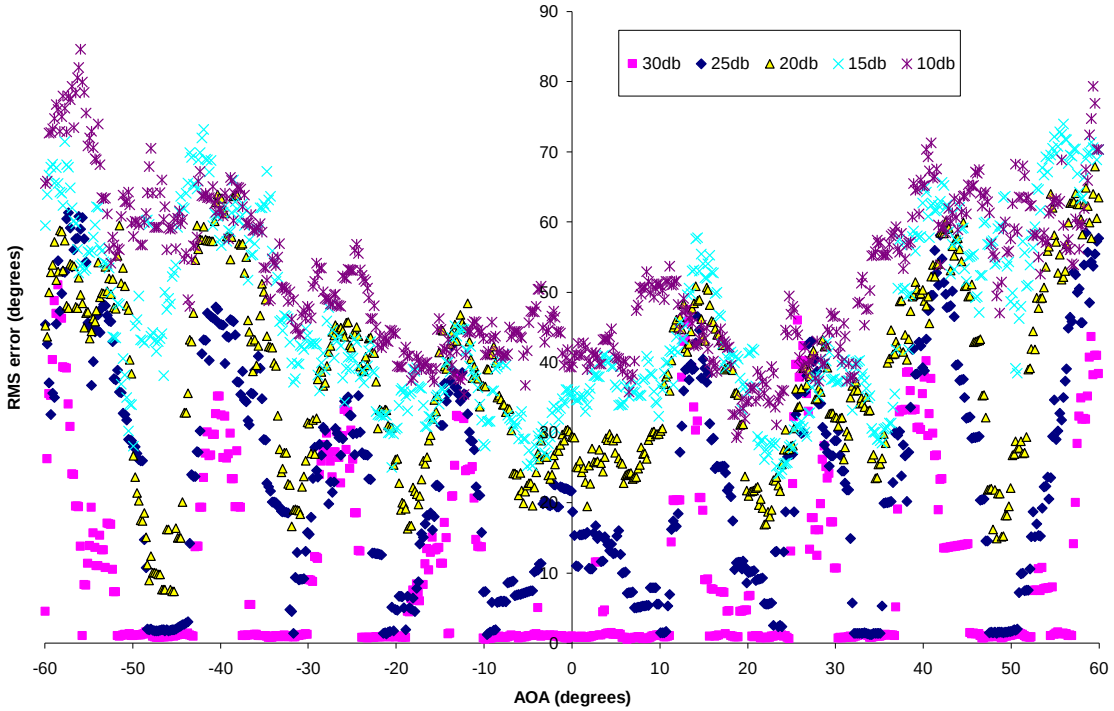

Figure 27. RMS error for 3 channels, $\widehat{M} = 426$, and SNRs from 10 dB to 30 dB

The RMS error for high SNR values is shown in Figures 27, 28, and 30. In Figure 27, the 3 channel data shows a bounded response with a high error value of 2.4°. The actual angular resolution for this dynamic range is 2.11°. Since most of the error values lay well below the broadside angular resolution, this result is favorable.

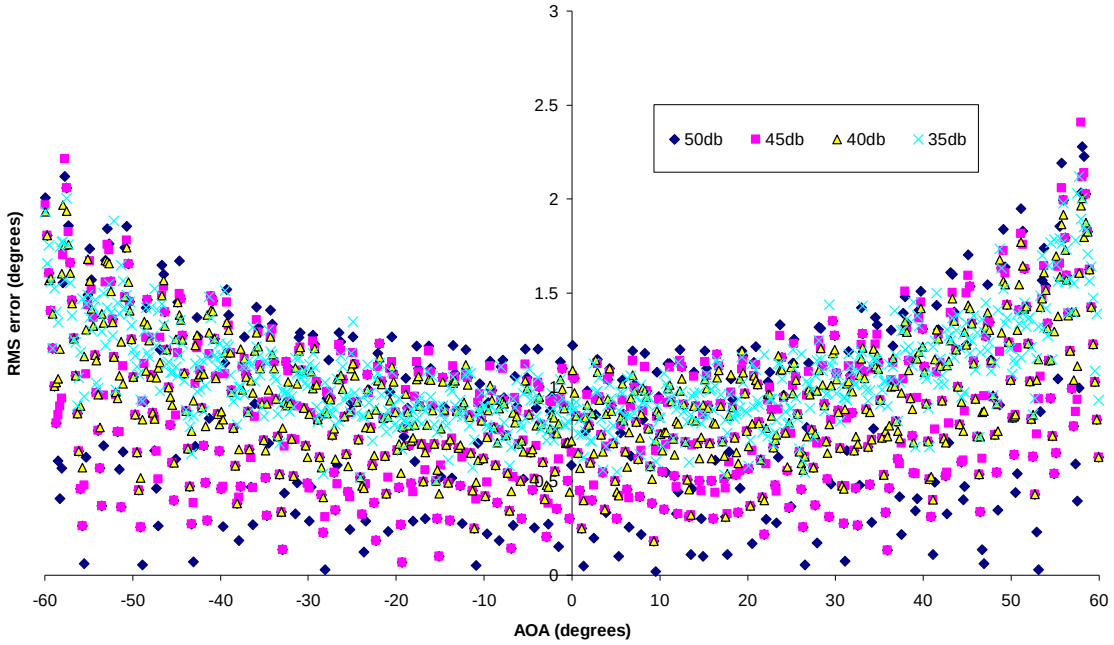

Figure 28. RMS error for 3 channels, $\widehat{M} = 85$, and SNRs from 35 dB to 50 dB

Figure 28 shows the error for 3 channels, $\widehat{M} = 276$. This data shows the periodic nature that was appearing in the low SNR data. This is an unfavorable response especially given the high values of the error. At SNR values above 40 dB the error is much more tolerable.

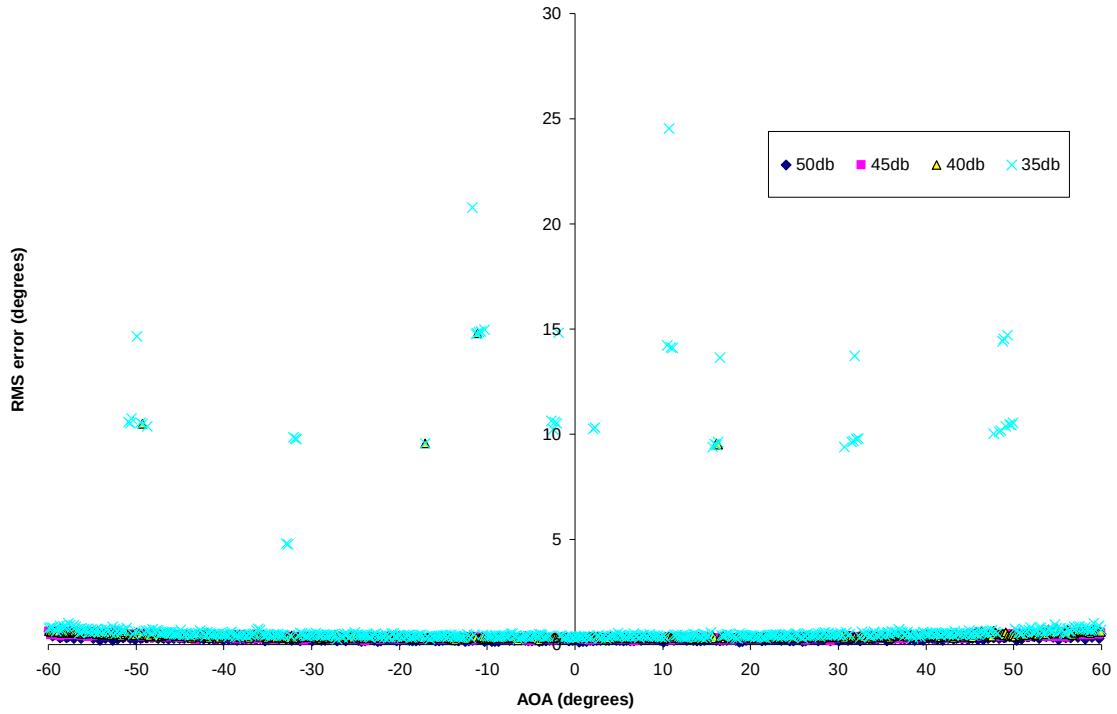

Figure 29. RMS error for 3 channels, $\widehat{M} = 276$, and SNRs from 35 dB to 50 dB

A linear log plot was produced for the data in Figure 28. Figure 29 shows that much of the data falls within the broadside angular resolution of 0.65°. On the log plot this equates to a value of -0.19. Only one of the SNR results are unusable, data for 40 dB have just a few points with high error but 45 dB and 50 dB are very good.

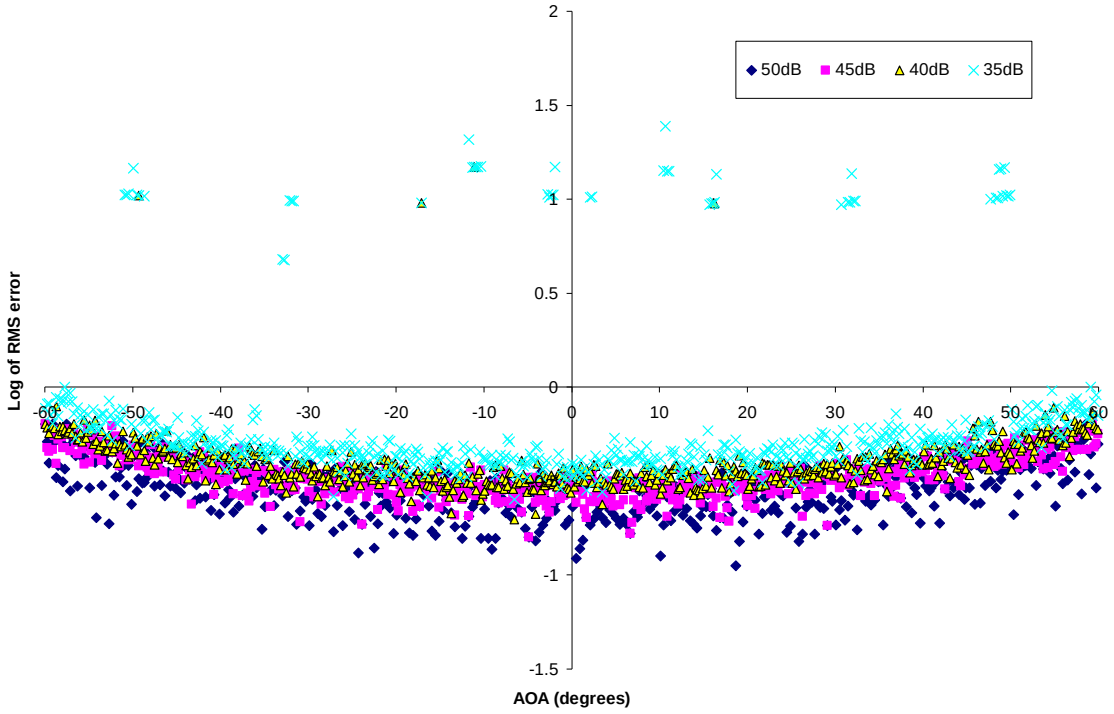

Figure 30. 3 channel Log of RMS error, $\widehat{M} = 276$, and SNRs from 35 dB to 50 dB

Figure 30 shows the error for 3 channels, $\widehat{M} = 426$. This data follows the trend from the low SNR cases in that these error values are worse than those in Figure 28. There is an especially bad error line from 40° to 45°.

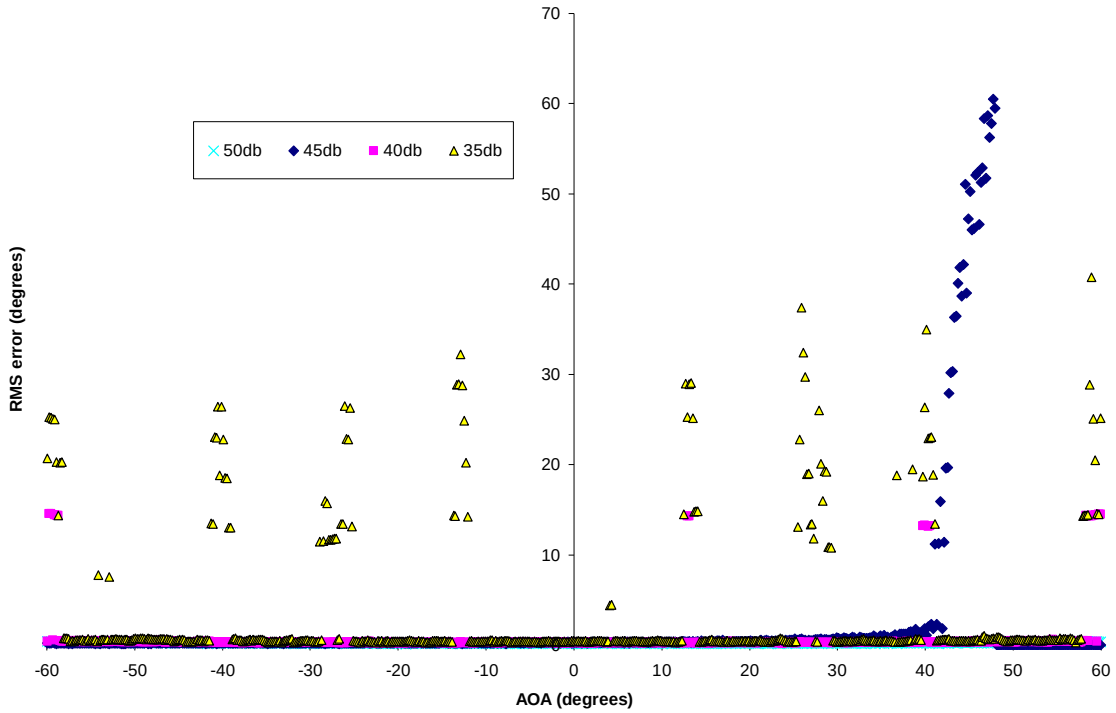

Figure 31. RMS error for 3 channels, $\widehat{M} = 426$, and SNRs from 35 dB to 50 dB

A linear log plot was produced for the data in Figure 30. Figure 31 shows that much of the data falls within the broadside angular resolution of 0.42°. On the log plot this equates to a value of -0.38. The data for the SNR of 45 dB exhibits a strange error around 40° which makes it unusable due to the requirement for good performance across the entire FOV. Data for 40 dB have just a few points with high error but 45 dB and 50 dB are very good.

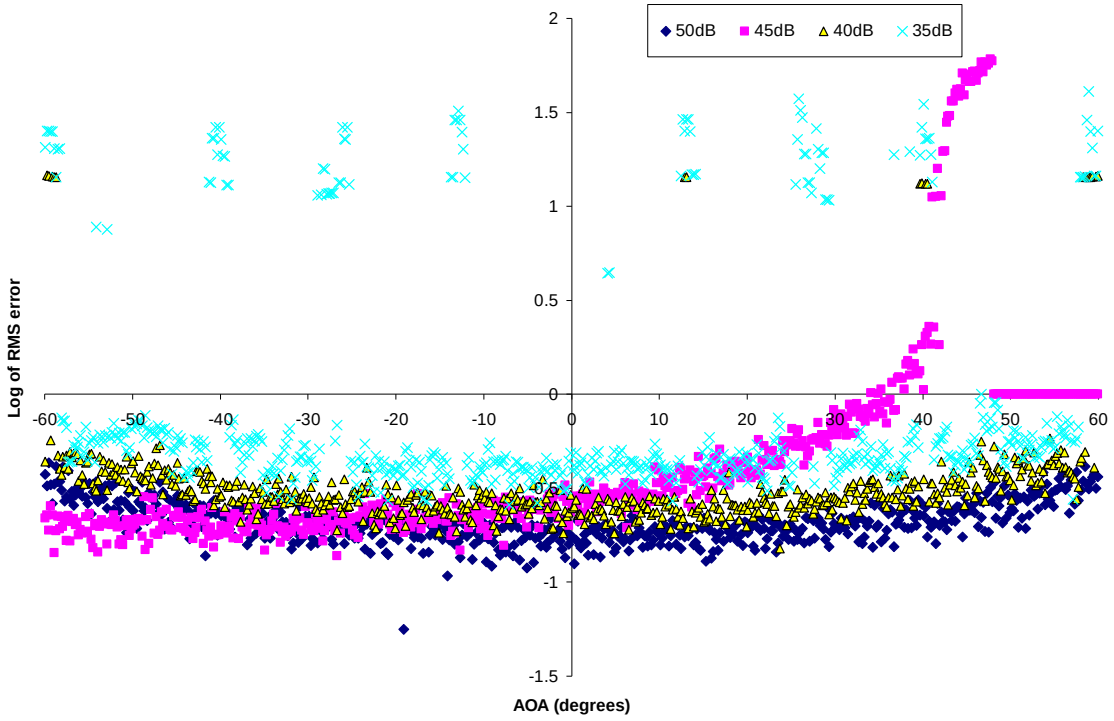

Figure 32. 3 channel Log of RMS error, $\widehat{M} = 426$, and SNRs from 35 dB to 50 dB

This dynamic range study showed that for the case of the chosen moduli sets, more channels are not always better. The 3 channel architecture yielded more favorable results than the 4 channel, and the 2 channel gave the best results especially in the $\pm 25^\circ$ range.

E. SUMMARY

This study was completed to better understand the relationship between the error and SNRs for 2, 3, and 4 channels. In general, it is expected that as long as the resolution (i.e. , $\widehat{M}$) is essentially the same, the performance in the presence of noise should also be about the same. The 2 channel moduli sets did very well when compared to their 3 and 4 channel counterparts. In some cases, the 4 channel data performed the worst over the whole SNR range. Overall, the small dynamic range moduli performed the best yielding the lowest error values especially in the 35 dB to 50 dB SNR range. The best for most of the SNR values was $\widehat{M} = 85$. Table 7 provides a quick view of the error results showing the high values for error in each of the SNR ranges.

	Small Dynamic Range			Large Dynamic Range			Comparison		
$\widehat{M}$	102	104	117	399	396	410	85	276	426
# channels	2	3	4	2	3	4	3	3	3
Broadside Angular Resolution (degrees)	1.76	1.73	1.54	0.45	0.45	0.44	2.11	0.65	0.42
RMS Error for SNRs from 10 dB to 30 dB (degrees)	47.0 (20 dB SNR)	74.3 (10 dB SNR)	74.3 (10 dB SNR)	78.1 (20 dB SNR)	86.2 (20 dB SNR)	84.3 (15 dB SNR)	91.1 (15 dB SNR)	77.3 (10 dB SNR)	80 (10 dB SNR)
RMS Error for SNRs from 35 dB to 50 dB (degrees)	1.53 (35 dB SNR)	1.98 (35 dB SNR)	1.19 (35 dB SNR)	65.2 (35 dB SNR)	27.4 (35 dB SNR)	35.0 (35 dB SNR)	2.4 (45 dB SNR)	24.5 (35 dB SNR)	60 (45 dB SNR)

Table 7. Simulation Summary Error Table

THIS PAGE INTENTIONALLY LEFT BLANK

V. HARDWARE TESTING

This chapter discusses the hardware design, testing procedures, and evaluation of the test results. There are two major aspects to the hardware testing. One is calibrating the demodulator boards, which are a critical component of the phase measurement. The second aspect is a bench top setup of a single channel RSNS array, where a phase shifted signal is input to a pair of demodulators, and then RSNS processing performed on the I and Q outputs.

A. HARDWARE SETUP

The hardware setup includes many pieces of equipment but the main components of the setup are the demodulator cards. A picture of the hardware setup and accompanying block diagram are given in Figure 32. A listing of the equipment used is in Table 8. The frequency of operation is 2.4 GHz.

Component Type	Quantity	Component Name
CW Frequency Source	1	HP 8341B Synthesized Sweeper
Power Splitter	4	Anaren 40266 2.4 GHz
Phase Shifter	2	Sage Laboratories Inc. DC-8 GHz
DC Power Supply	1	Condor GL50A 50Watt CH1 5.05VDC 4A, CH2 12VDC 2.5A, and CH3 -12VDC 0.2A
Cable	19	Pasternek Cable RG-306
Variable Attenuator	1	Telonic Altair Attenuation Model 8140S
Demodulator Board [TST1, TST2]	2	AD 8347 Demodulator Board
Amplifier	2	Differential Amplifier with LPF bandpass 3 dB of 10 MHz and Voltage gain of 10
Computer	1	NI PXIe-1062Q
Digital Oscilloscope Cards [DAQ 2, DAQ 3]	2	NI PXI-5112 100 MHz Digital Oscilloscope 8-bits, ± 10 Volts range (adjustable)

Table 8. Hardware Equipment List

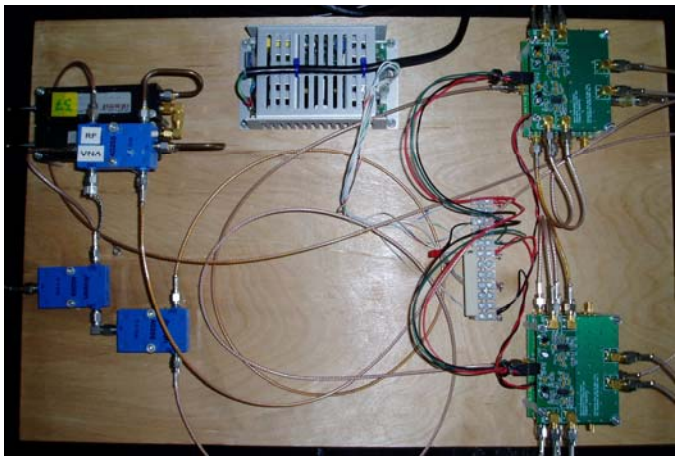

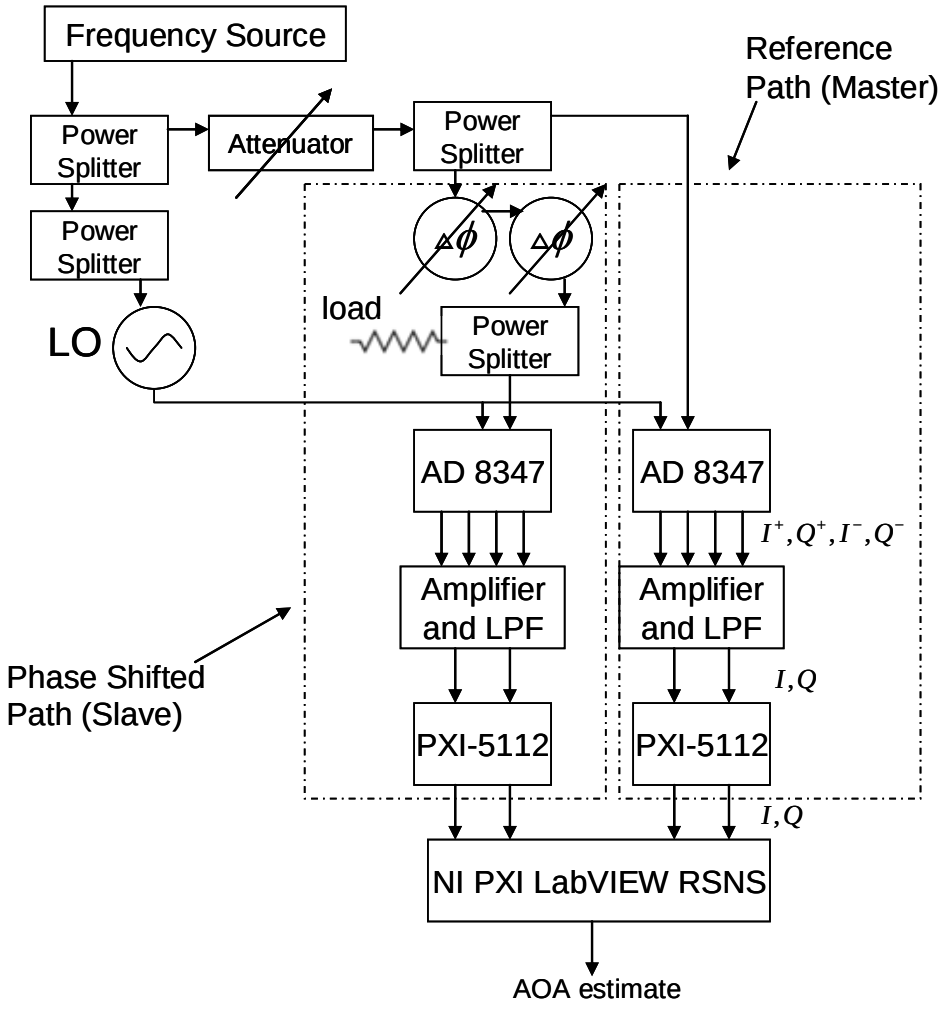

Figure 33. Laboratory Hardware Setup and Block Diagram

B. CALIBRATION

The demodulator boards have an inherent direct current (DC) voltage offset. This needs to be accounted for before the RSNS processing in order to have accurate AOA results for the system. To find this offset, a calibration was performed. This calibration was first described in [13].

With the equipment set up as described in Figure 32, the I and Q quadrature outputs were input into the NI PXI-5112 Oscilloscope card on the NI PXIe-1062Q. Both of the NI PXI-5112 Oscilloscope cards had to be calibrated using software in the LabVIEW library before any measurements were taken.

A LabVIEW program was fed the I and Q voltages from the bench top setup and the I/Q plot was generated. The calibration program was written to take one record of data at a constant phase. The user sets the phase before starting the program. This program takes $10,000$ points at a time and computes the mean values for I and Q which are then saved to a file. The user then changes the phase and repeats the process until all 360° of phase shift are covered and a complete set of data points taken. The first half of the program as discussed is shown in Figure 33.

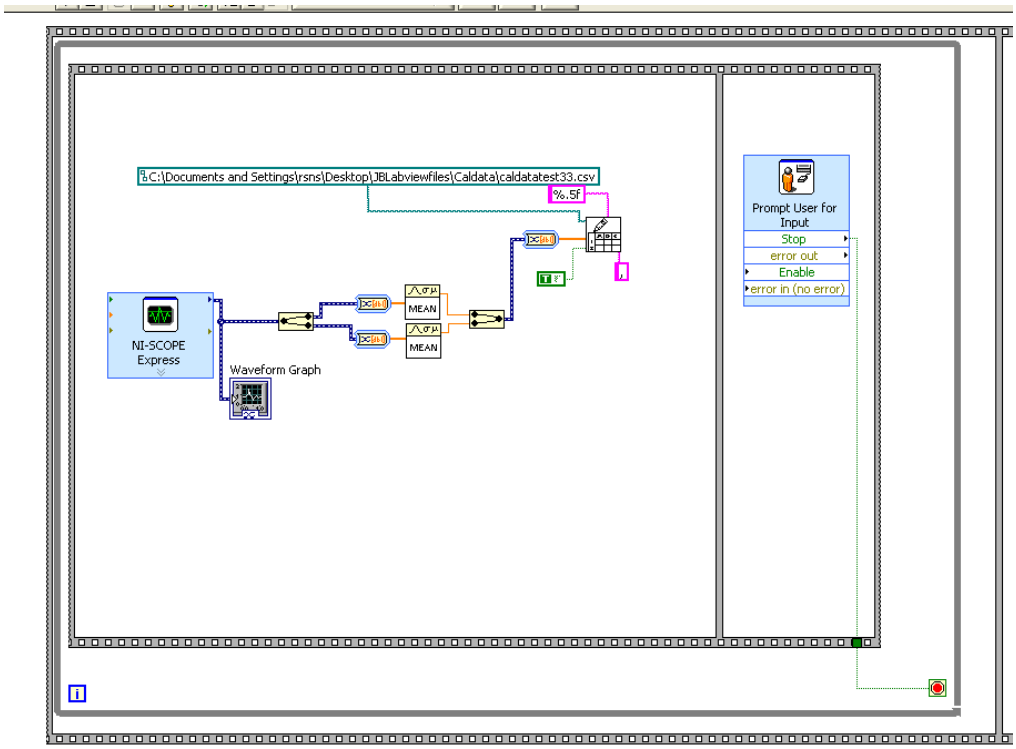

Figure 34. LabVIEW data collection part of calibration program

The user stops this phase collection operation and the program recalls the raw data, graphs the original I and Q values, calculates the mean value of all the I and Q data, and outputs a new graph centered at zero. The centered I/Q circle (data with the offsets subtracted) is also displayed. The portion of the LabVIEW program that accomplished this is shown in Figure 34.

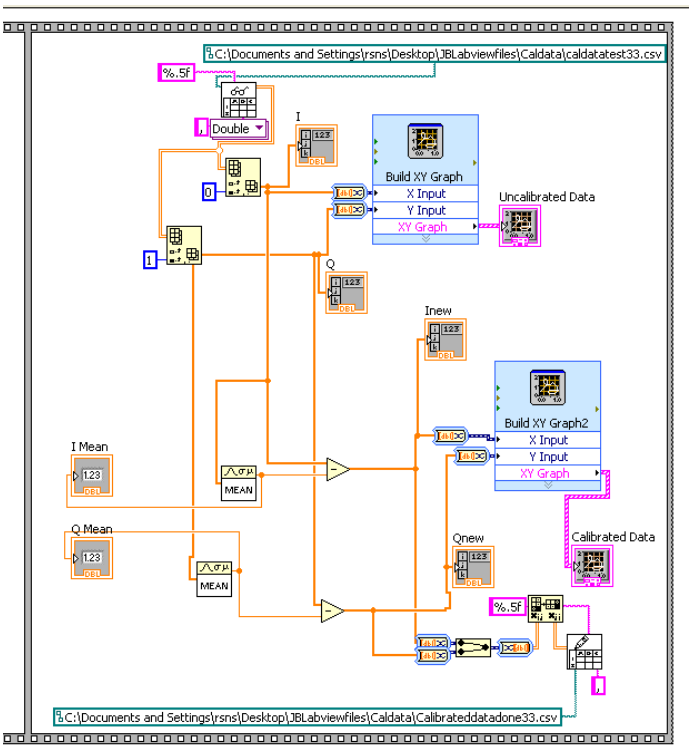

Figure 35. LabVIEW calculation part of calibration program

Before the calibration is started, adjustments should be made to the power levels to ensure that components were not being over driven or under driven [14]. The settings used are shown below in Table 9.

Operating Frequency	2.4 GHz CW
HP output	3.00 dBm
LO level	-7.4 dBm
RFIN phase shifted	-46.6 dBm
RFIN not shifted	-41.4 dBm

Table 9. Equipment Measurement Settings

The I and Q offset values for each board are listed in Table 10, giving offsets for three attenuation values on the variable attenuator: 23 dB, 33 dB, and 43 dB. These values represent the range over which the demodulators yield valid results. This equates to a 30 dB dynamic range.

Board	TST 1 (Board 1)			TST 2 (Board 2)		
Attenuation	23 dB	33 dB	43 dB	23 dB	33 dB	43 dB
I (V)	–0.5414 V	–0.5766 V	–0.5778 V	–0.5927 V	–0.5853 V	–0.5805 V
Q (V)	–0.3336 V	–0.3169 V	–0.3234 V	–0.1450 V	–0.1578 V	–0.1603 V

Table 10. I and Q offset values

The calibration screenshot is presented for TST1 (demodulator board 1) in Figure 35 and for TST2 (demodulator board 2) in Figure 36. For the remainder of the research, the offset values for the 33 dB attenuation were used in the LabVIEW programs.

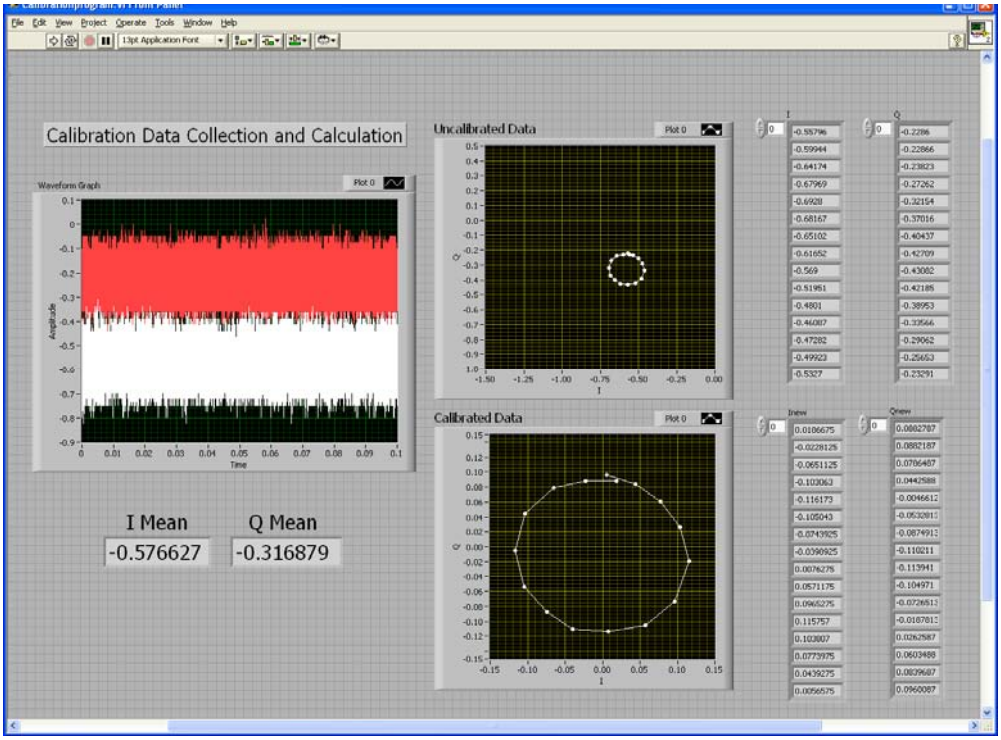

Figure 36. Calibration data for TST1 (Demodulator Board 1)

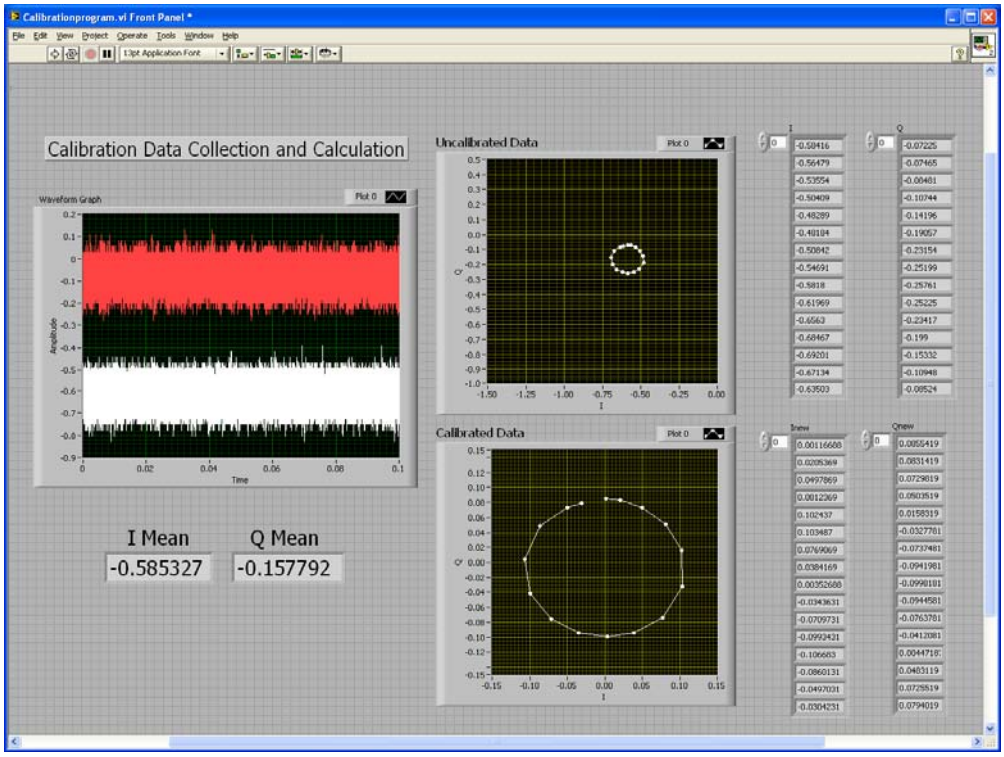

Figure 37. Calibration data for TST2 (Demodulator Board 2)

C. RSNS IN LABVIEW

LabVIEW was also used for the bench top implementation of the RSNS array. It controlled the two NI PXI-5112 cards as described in Section B. The program consisted of two major parts and was run using the RSNS moduli set [5 9].

The first part synchronizes the outputs from the two cards [15] to ensure the data is matched up correctly as it came in off the lab setup. The master in this case is the demodulator card TST2 coming off the DAQ-2, NI PXI-5112 card. The slave is the demodulator card TST1 off the DAQ-3, NI PXI-5112 card. The slave is the card that is injected with the phase shift. Figure 37 shows the data coming in from the master and slave and passing through the NI scope utilities.

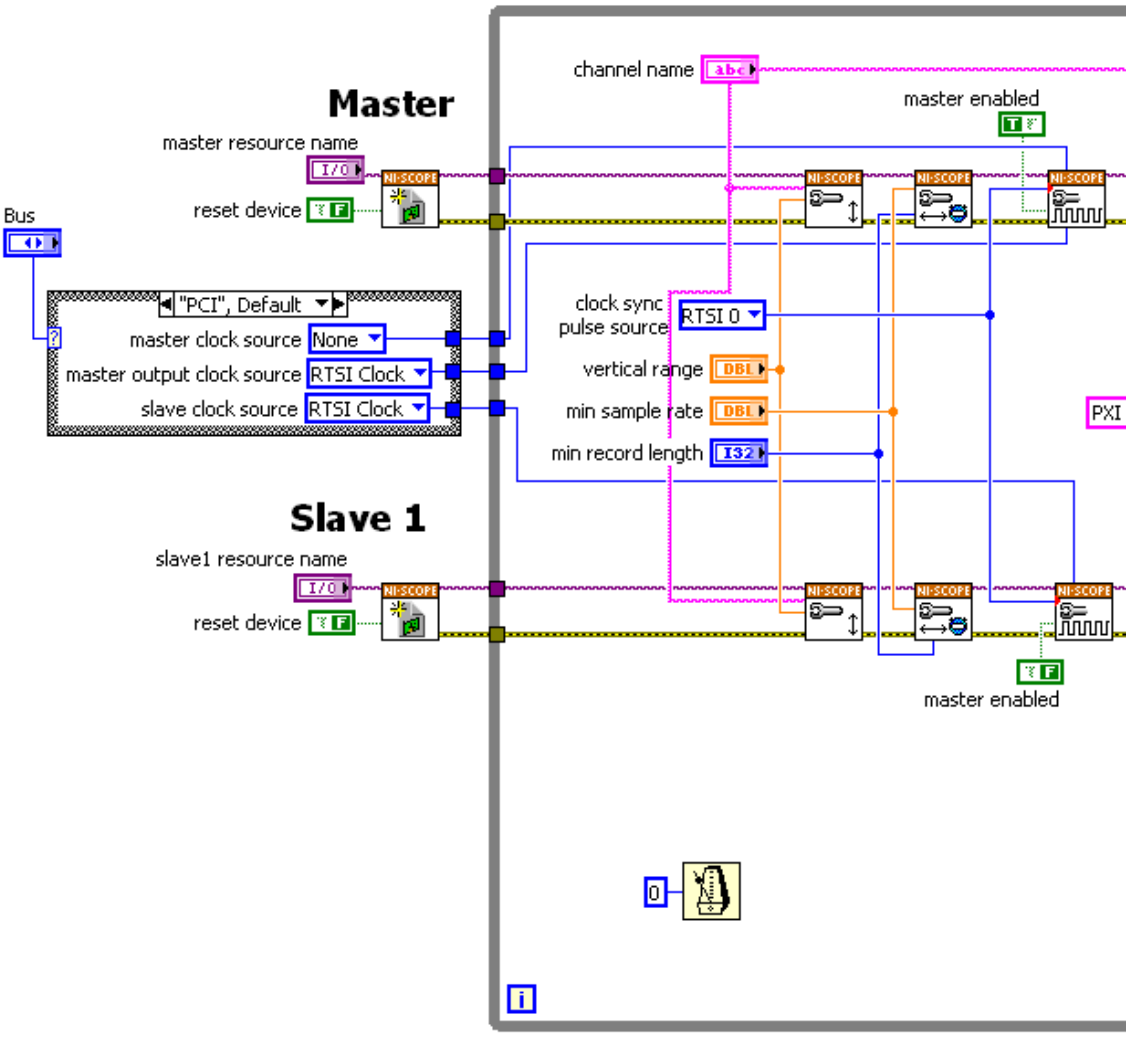

Figure 38. First part of DF program showing master and slave data flow

An immediate trigger is used in this program for continued and accurate triggering. Figure 38 shows the data passing through the master trigger that then passed the triggering information on to the slave trigger. This data is then piped through in a cluster format until being separated into I and Q values before being converted to waveform data.

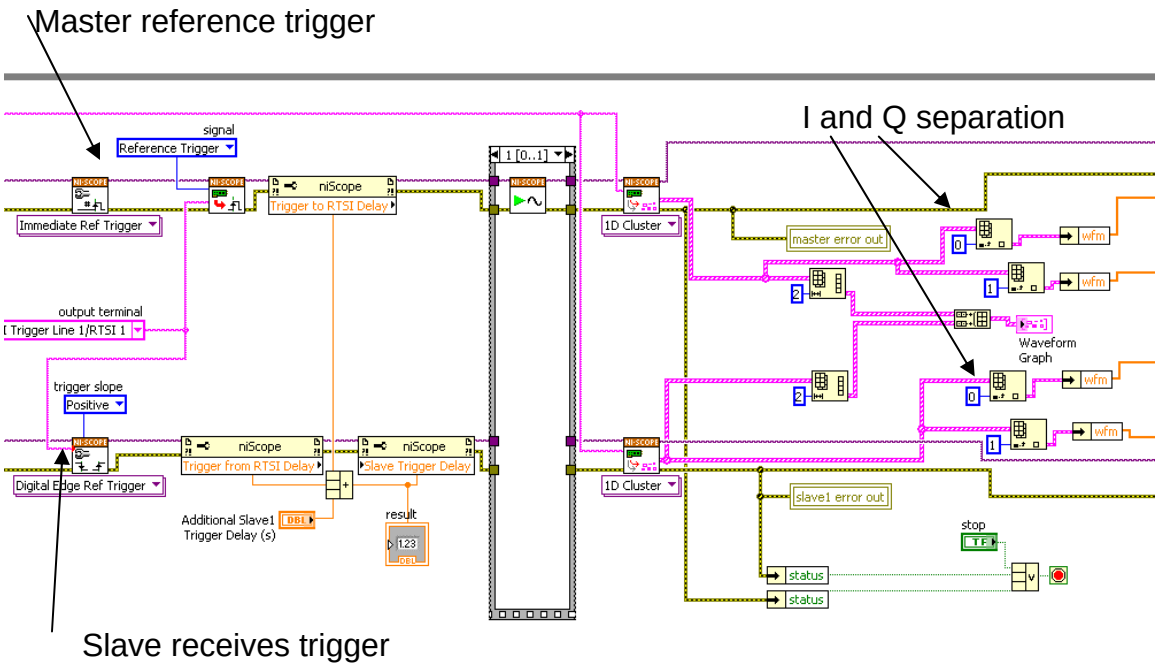

Figure 39. Second part of DF program data triggering and conversion

Then the program routes the I and Q data to a mean calculation where $10,000$ points are averaged. The I and Q offset from the calibration step is then subtracted from I and Q values from both boards shown in Figure 38. These calibrated values are then fed to the second part of the program shown in Figure 39.

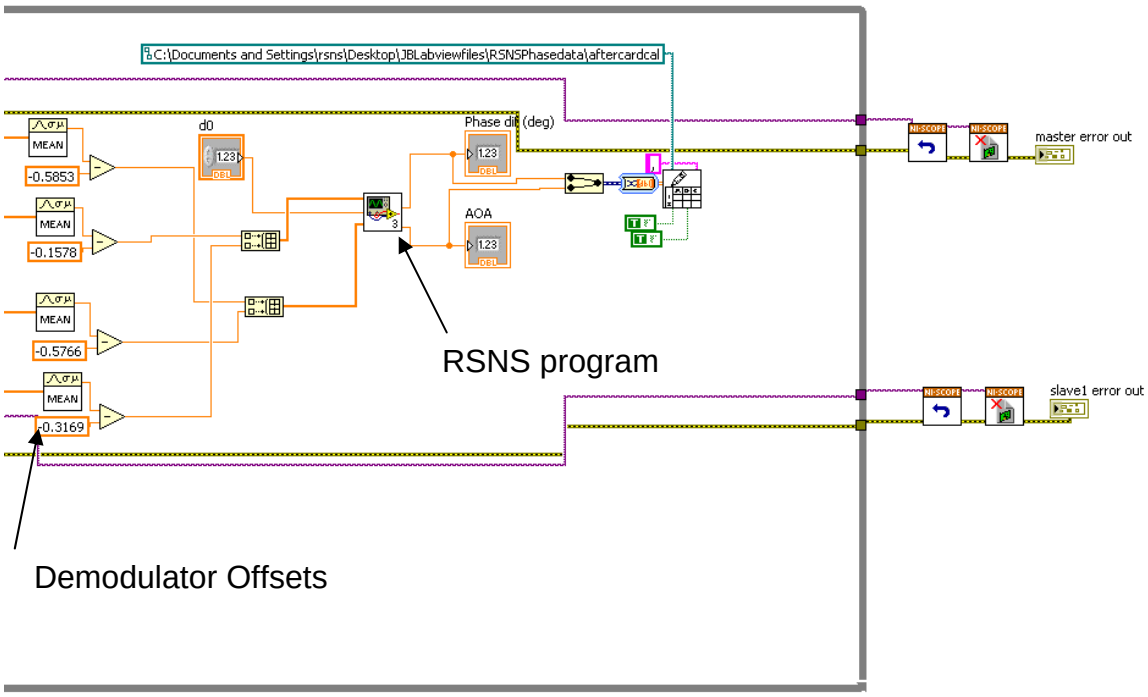

Figure 40. Last part of DF program averaging I and Q and passing to RSNS

The RSNS takes the I and Q values and calculates the phase data. A correction factor to center the data is applied to both I and Q values. The element phase and phase difference terms are displayed. The phase difference data are used in the calculation of the folding waveforms as shown in Figure 40. The folding waveforms are scaled according to the virtual spacings and then aligned using the required phase shifts, ς_i. For the bench top setup, the physical spacing was set to $d0 = \frac{\lambda}{2}$.

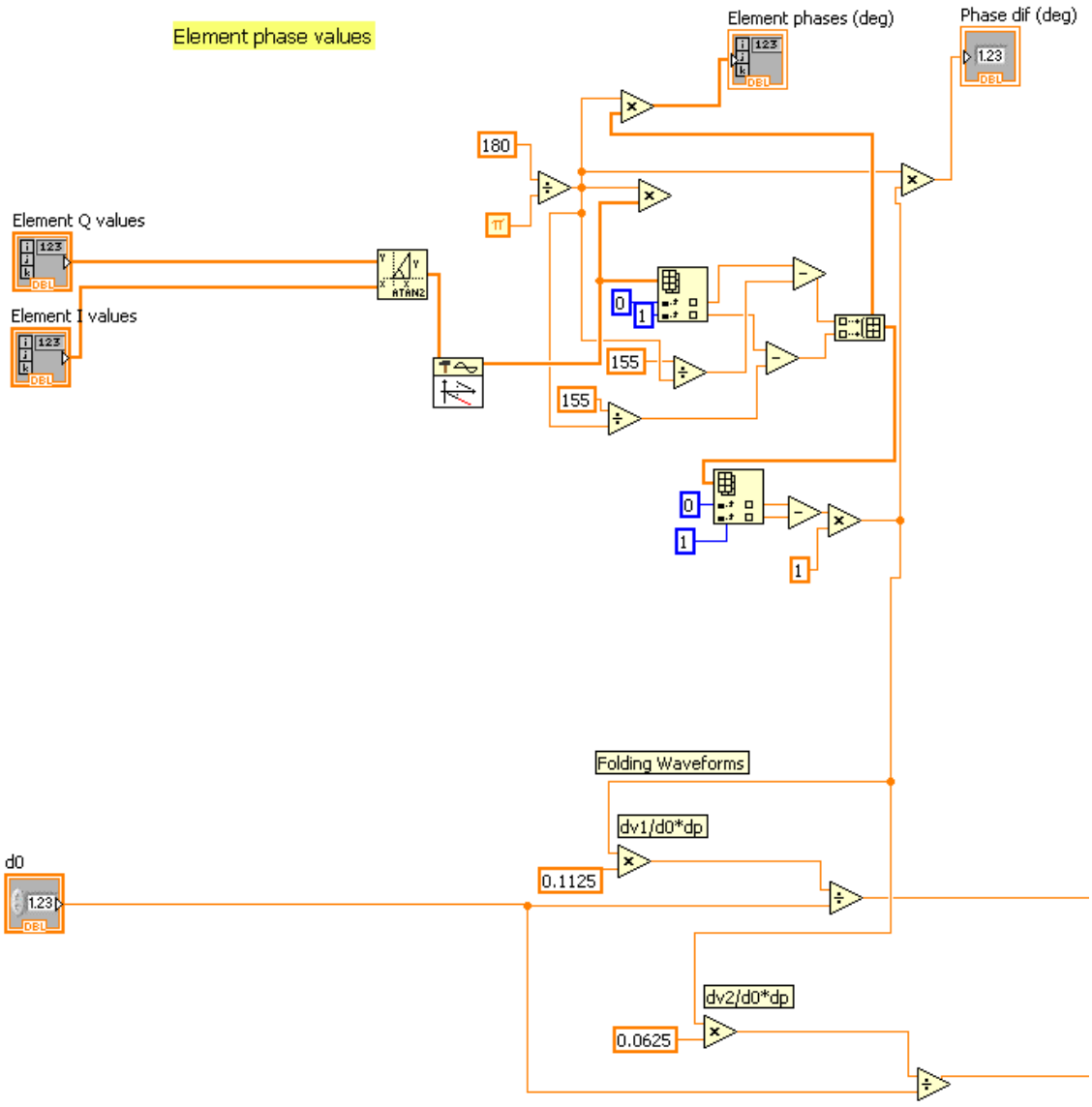

Figure 41. RSNS module phase and folding waveform calculations (part1)

Once this is completed, the folding waveforms are generated for virtual channels and then compared with the RSNS thresholds as shown in Figure 41.

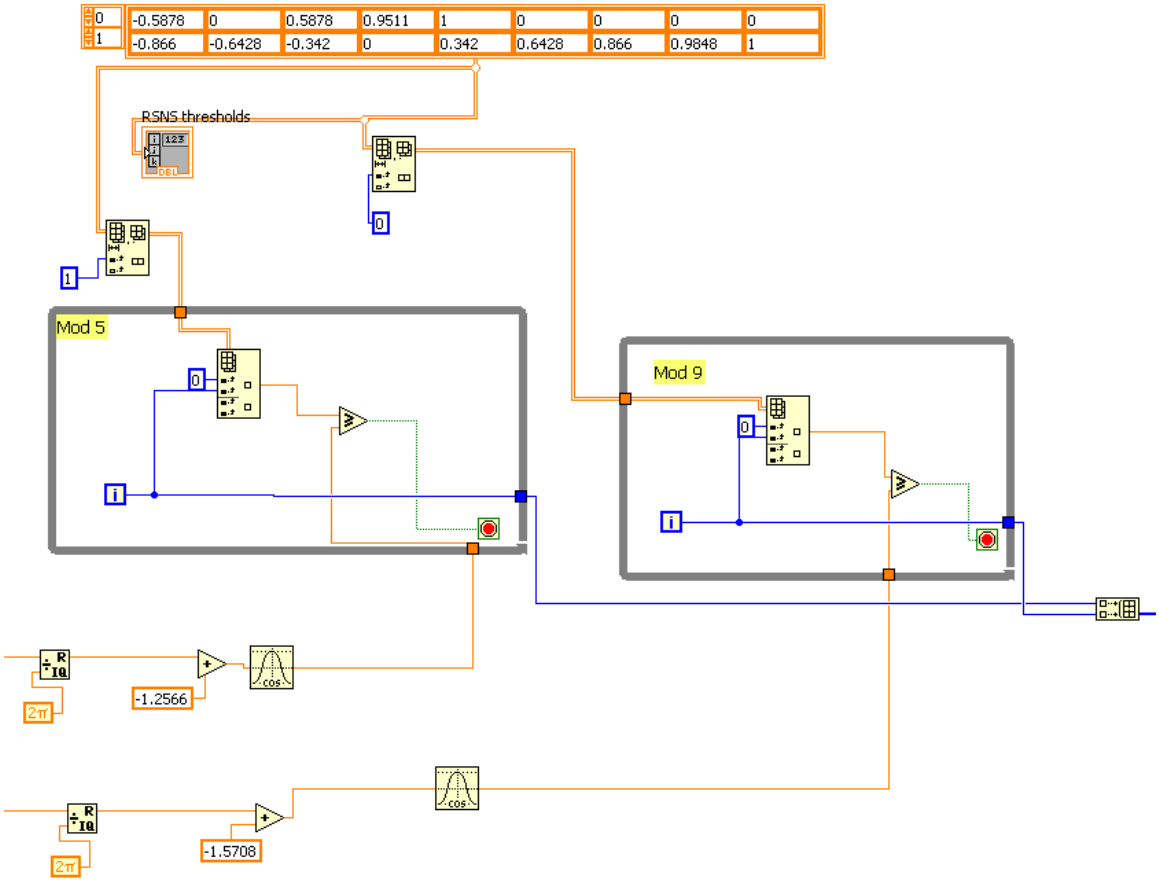

Figure 42. RSNS threshold values

Figure 42 shows the thresholded outputs being compared to the RSNS code, and finally returning AOA estimates.

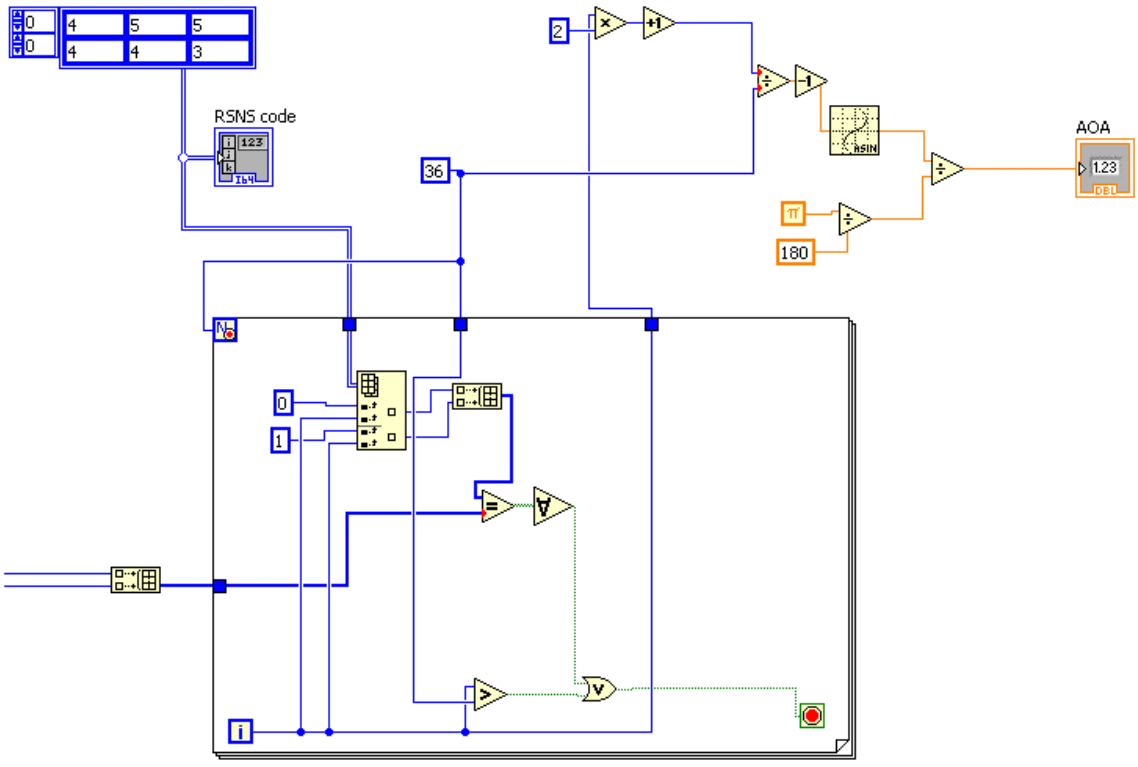

Figure 43. RSNS code and AOA calculation

D. RESULTS

The LabVIEW program from Section C was run to collect the data. The phase shifters were turned in approximately 6° steps for a total 360° of phase shift. After the data was collected, a new portion of the program was run to plot the data in Figure 43. The results from the RSNS program give estimated AOA and measured phase difference. The desired plot is estimated AOA vs real AOA. Because plane wave excitation was not used there is no AOA per se, but the measured phase shift was available. The actual phase shift being injected into the equipment could not be measured because of power limitations on the network analyzer. A spot check was completed that ensured the phase shift measured equaled the phase shift injected, but this could not be done to a high precision. To achieved the appropriate plot, the simulated AOA was calculated using a rearranged version of Equation (2.3),

$$\text{simulated AOA} = \sin^{-1}\left(\frac{\triangle\phi}{kd}\right) \tag{5.1}$$

where $d = \frac{\lambda}{2}$ for measured data in the range $-180^{\circ} \leq \triangle\phi \leq 180^{\circ}$.

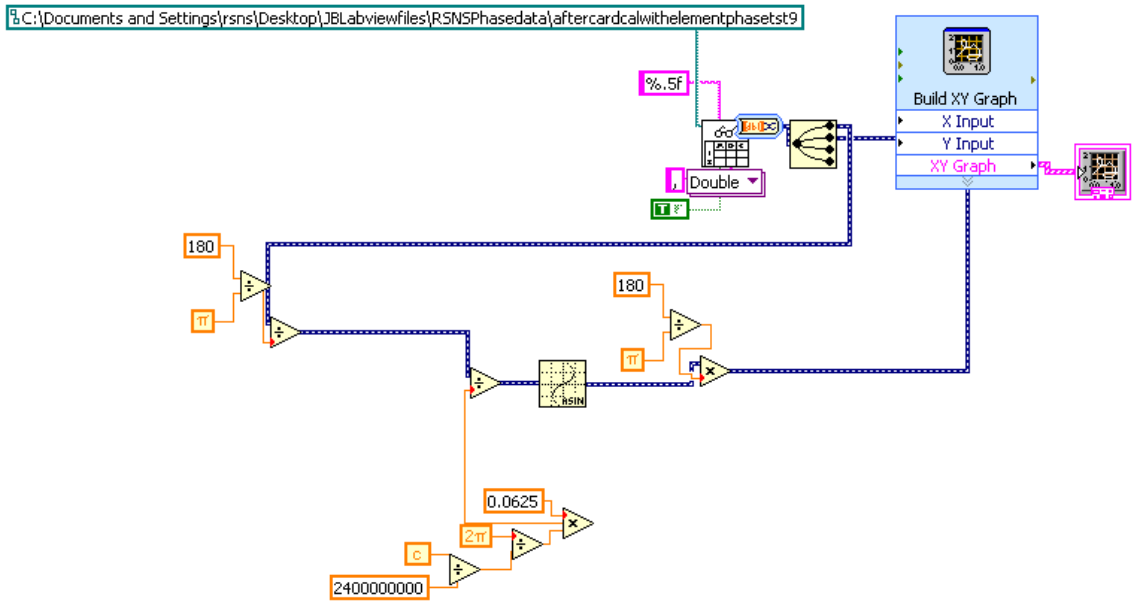

Figure 44. Plot program for estimated AOA vs simulated AOA

The raw phase data is shown in Figure 44. The data shows a phase shift of approximately 360°. The data near the two endpoint shows variation which is likely due to the phase shifters hitting the stops at the two ends.

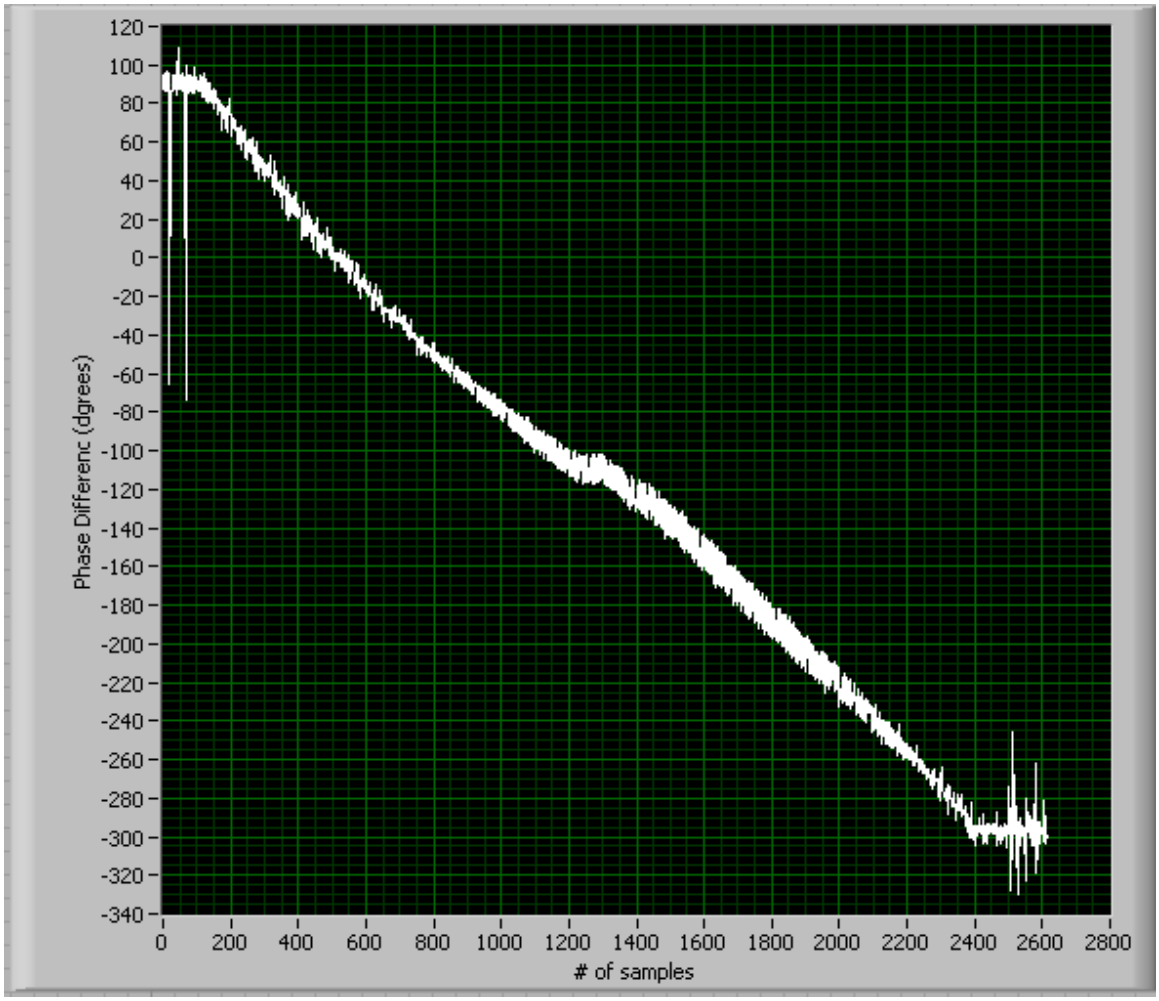

Figure 45. Measured Phase Data

Figure 45 plots the measured phase data versus estimated AOA. The data appears as expected with a smooth steps from $\pm 90^{\circ}$.

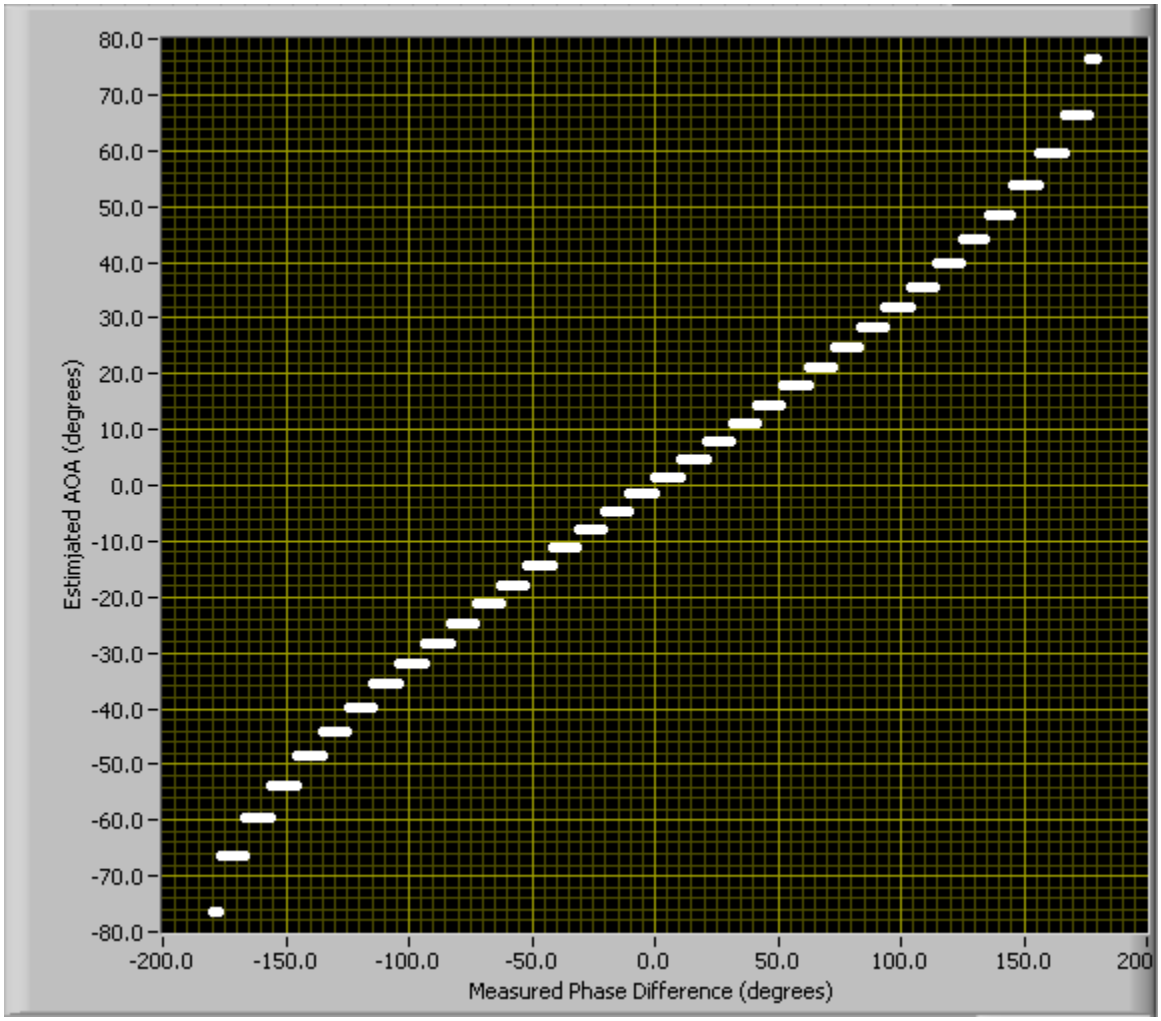

Figure 46. RSNS Measured Phase Difference vs Estimated AOA

The estimated AOA versus simulated AOA is plotted in Figure 46. These results show that the single channel theory is valid and the results are as expected. There is a noticeable increase in bin size as the AOA nears $\pm 90^{\circ}$ and the results follow linear behavior. These experimental results match those of the example in Figure 6 very well. The data presented here is a high SNR case, while the exact SNR is unknown, it is presumed to be close to 50 dB based on the specifications for the automatic gain control (AGC) on the demodulator boards [14].

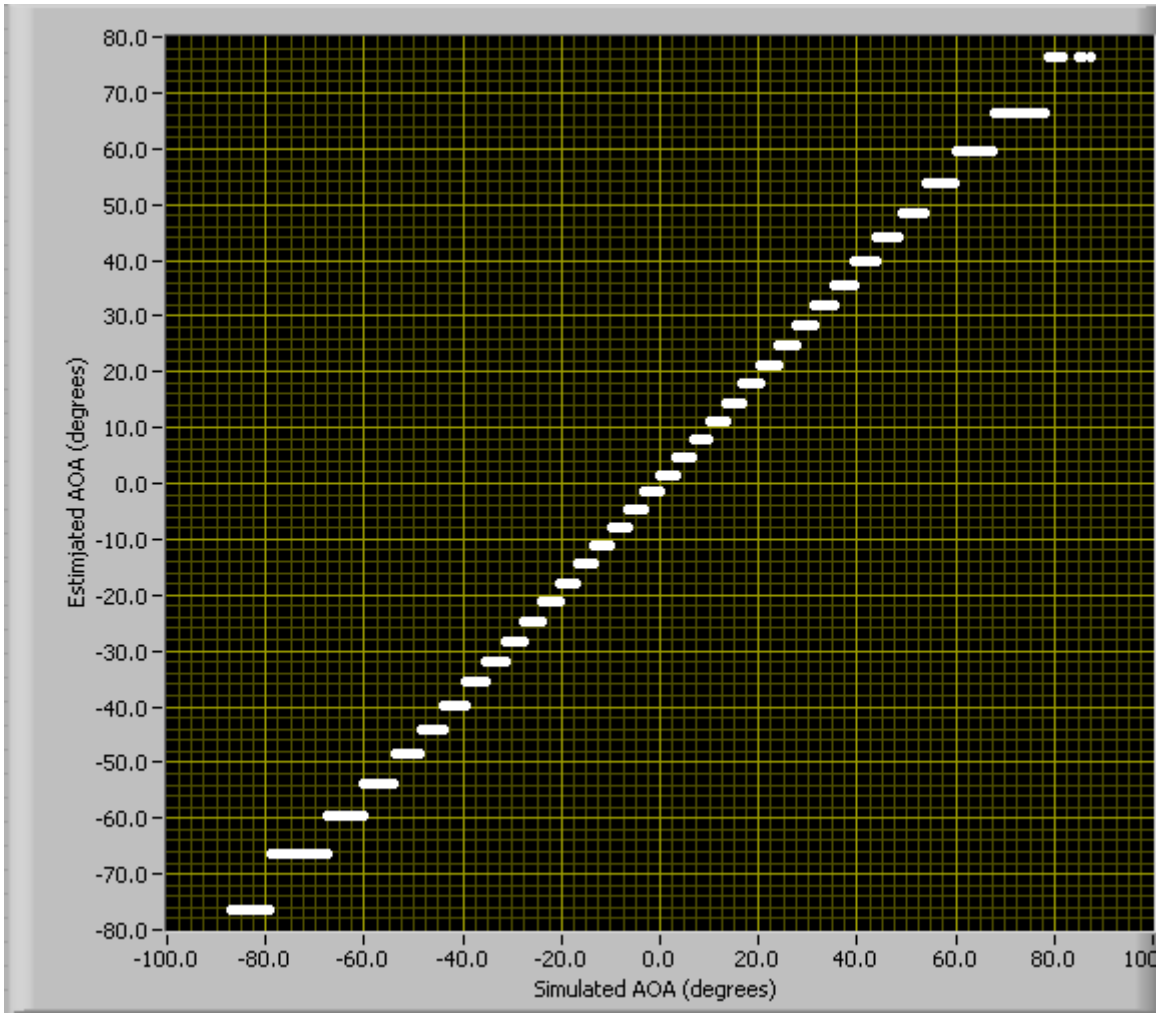

Figure 47. RSNS Estimated AOA Transfer Function

For comparison purposes, the transfer functions and simulations were run for $\widehat{M} = 36$ with moduli of [5 9] at SNRs of 10 dB, 25 dB, and 50 dB. The transfer function in Figure 47 is for the SNR of 10 dB. The dashed blue line represents a perfect match between estimated AOA and real AOA. The data for this 10 dB case is very scattered and does not give a good correlation.

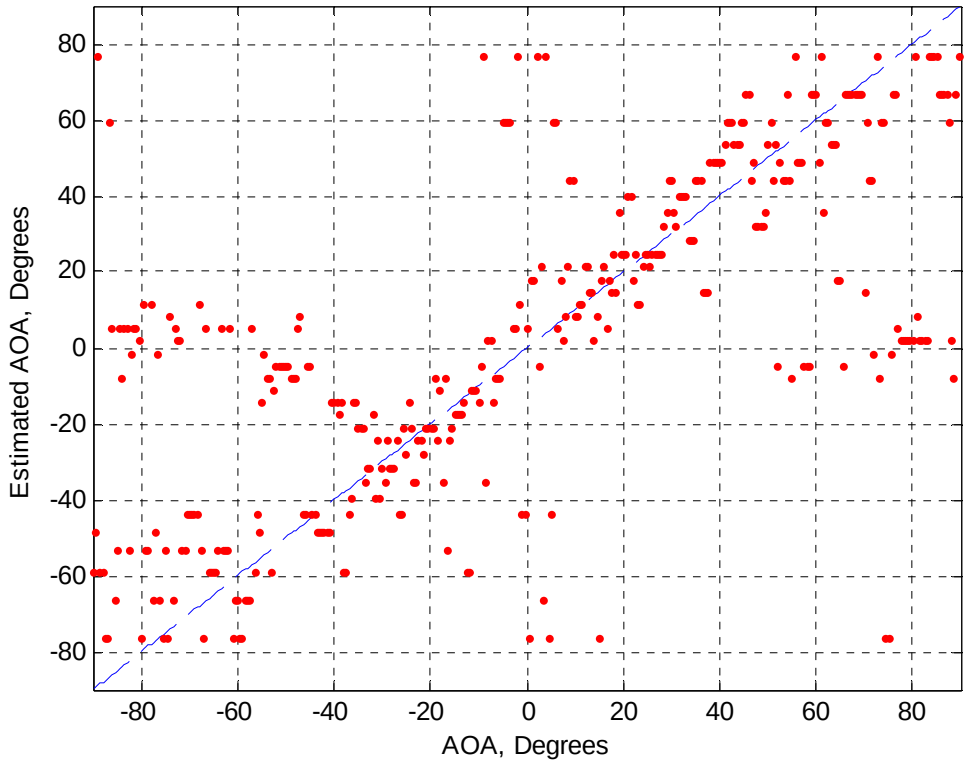

Figure 48. Simulated AOA Transfer Function, $\widehat{M} = 36$, and SNR of 10 dB

The transfer function in Figure 48 is for the SNR of 25 dB. The data for this 25 dB case is much improved from Figure 47. The data follows the ideal line much more closely.

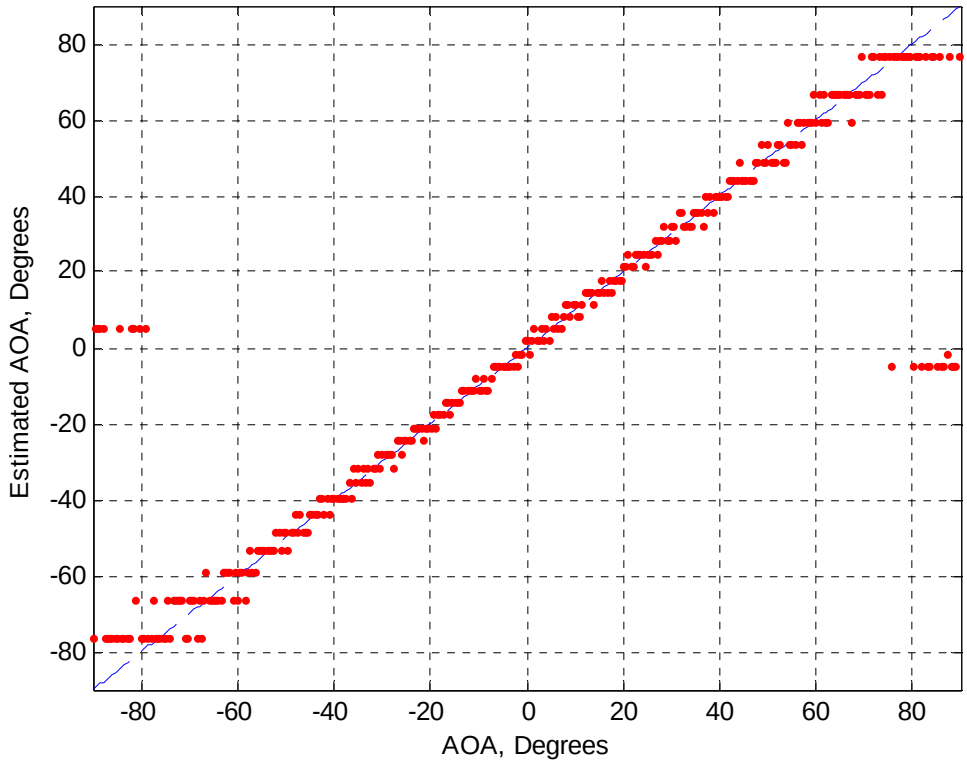

Figure 49. Simulated AOA Transfer Function, $\widehat{M} = 36$, and SNR of 25 dB

The final transfer function in Figure 49 is for the SNR of 50 dB. The data for this 50 dB case is the best out of the three showing excellent correlation. This transfer function is a near perfect match to the experimental data in Figure 46.

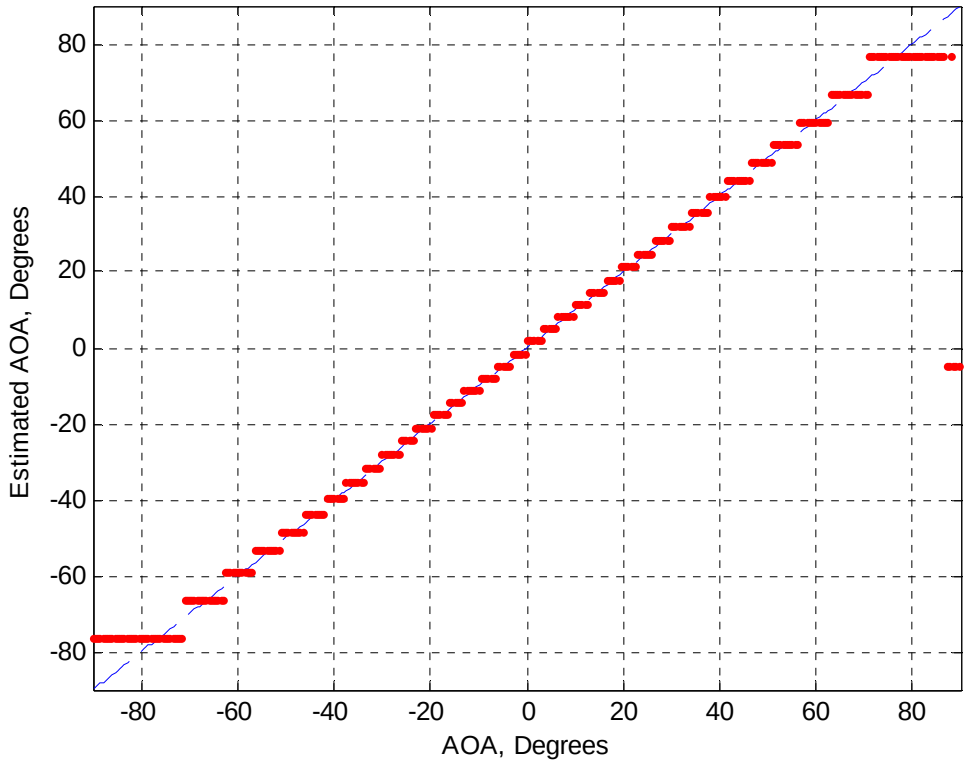

Figure 50. Simulated AOA Transfer Function, $\widehat{M} = 36$, and SNR of 50 dB

Next the simulation was run for 10 dB, 25 dB, and 50 dB. Figure 50 plots the RMS error. The broadside angular resolution for $\widehat{M} = 36$ is 5°. The error in the 10 dB case falls well above this value. The data for 25 dB and 50 dB is more reasonable, but the 25 dB case has significantly higher error around 0°.

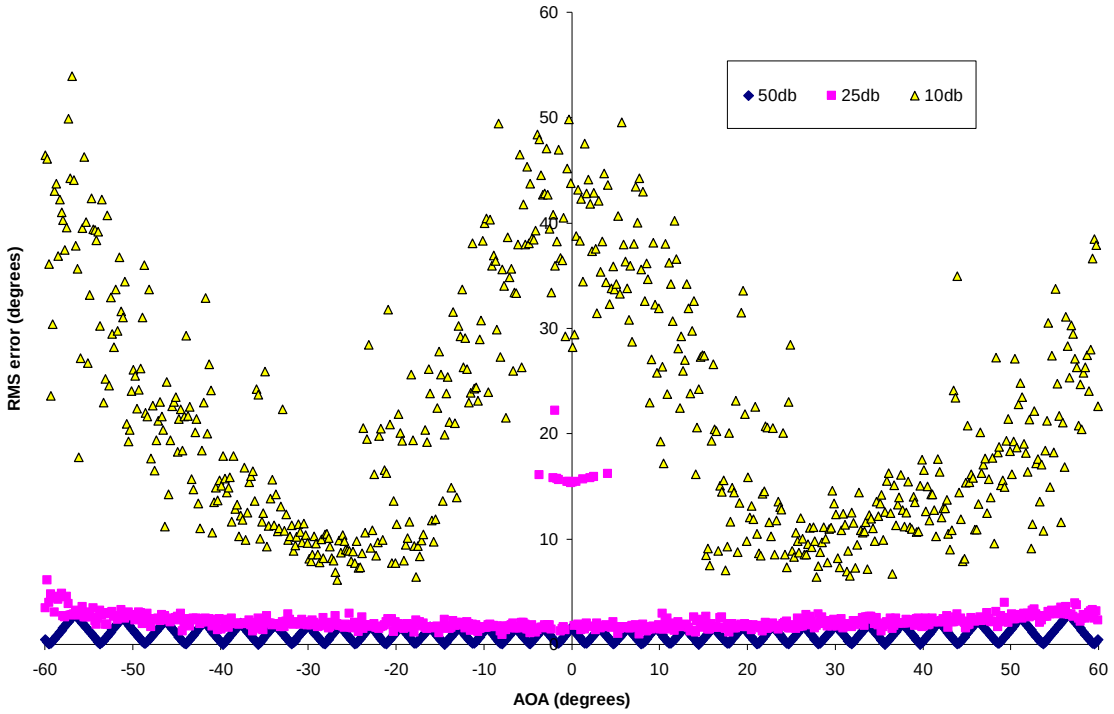

Figure 51. 2 channel RMS error, $\widehat{M} = 36$, and SNRs of 10 dB, 25 dB, and 50 dB

A linear log plot was produced for the data in Figure 50. Figure 51 shows that two out of the three SNRs fall within the broadside angular resolution of 5°. On the log plot this corresponds to a value of 0.70. The data for the SNR of 10 dB is almost completely out of the usable range.

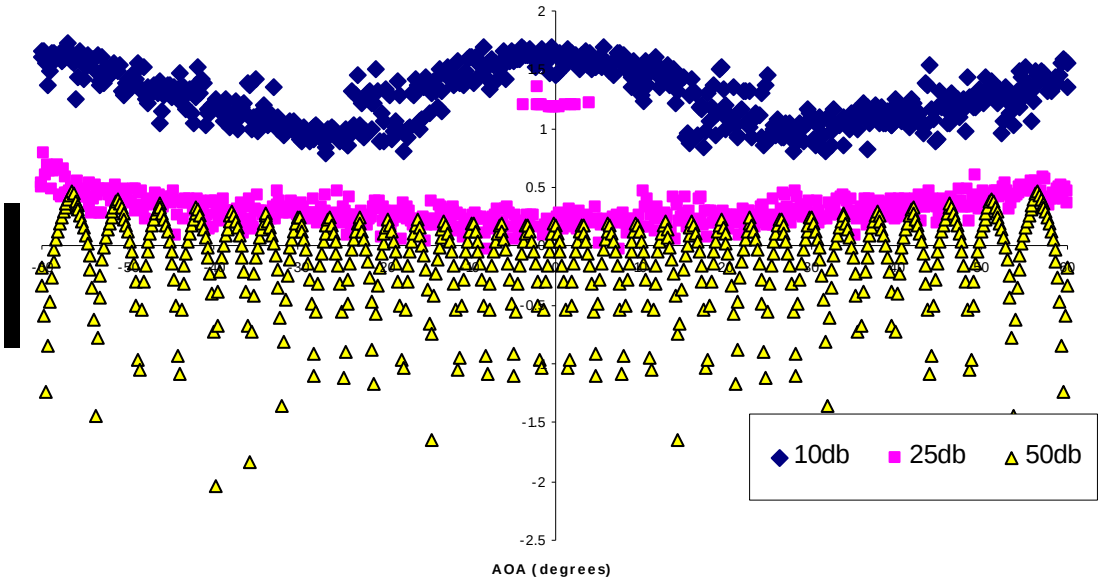

Figure 52. 2 channel Log(RMS error), $\widehat{M} = 36$, and SNRs of 10 dB, 25 dB, and 50 dB

E. SUMMARY

In this chapter, the hardware and software used for implementation of the RSNS DF system were described. The block diagram laid out the hardware used. Calibration was completed on the demodulator boards. The hardware and LabVIEW software were combined for the RSNS DF system to be bench tested. The expected results were achieved and compared to the simulated transfer function. In the next chapter, concluding remarks and suggestions for future work will be discussed.

THIS PAGE INTENTIONALLY LEFT BLANK

VI. CONCLUSIONS AND RECOMMENDATIONS

This chapter summarizes the contributions of this thesis and makes conclusions on the results. Recommendations for future work are also made.

A. SIMULATION RESULTS

Simulations were done for three sets of moduli to determine the effects of random noise. The study found that for the small dynamic range values, viable results occurred for most moduli sets for SNRs from 35 dB to 50 dB. The highest error values within these SNRs was either within or slightly above the broadside angular resolutions for each moduli set, and there was no significant difference between 2, 3, and 4 channel data.

The large dynamic range values yielded more disappointing results. The difference in error did not significantly change with channel number. In these sets, the viable data occurred from 45 dB to 50 dB.

The 3 channel dynamic range study yielded the most interesting results. In this case, the small dynamic range gave viable results for SNRs of 25 dB to 50 dB while the medium dynamic range results were good for SNRs of 40 dB to 50 dB and the large dynamic range results were only good for SNRs of 50 dB.

This study showed that the small dynamic range moduli performed the best for the largest range of SNRs. Whether there were 2, 3, or 4 channels was immaterial in the results. The overall best error results came for $\widehat{M} = 85$.

B. HARDWARE RESULTS

The demodulator boards were calibrated and the resulting offsets were used in the LabVIEW program. The estimated AOA results were as expected. A linear plot was achieved and the bin sizes varied with AOA as expected. The experimental results matched those produced from the simulation with a high correlation.

C. RECOMMENDATIONS AND FUTURE WORK

Future work for the simulations would be to run more studies with different scaling factors. Another study could implement the use of the Cramér Rao bound for error estimation as in [16].

There are many opportunities for future work with the hardware. This thesis stopped short of applying this hardware to a two element antenna array. The two element array could be tested using the RSNS code in an anechoic facility. After satisfactory results there, the setup could be tested in an outdoor environment.

LIST OF REFERENCES

[1] Hendon H. Jenkins, *Small-Aperture Radio-Direction Finding,* pp 1, 11-18, Artech House, Norwood, Massachusetts, 1991.

[2] Anthony Lee, "Variable Resolution Direction Finding using the Robust Symmetrical Number System," Master's Thesis, Naval Postgraduate School, Monterey, California, December 2006.

[3] David J. Wickersham, "Application of the Robust Symmetrical Number System to High Resolution Direction Finding Interferometry," Master's Thesis, Naval Postgraduate School, Monterey, California, March 2000.

[4] Y. W. Wu, S. Rhodes, and E. H. Satorius, "Direction of Arrival Estimation Via Extended Phase Interferometry," *IEEE Transactions on Aerospace and Electronic Systems,* Vol. 31, No. 1, pp.375-382, January 1995.

[5] W. A. U. Titze, P. V. Brennan, and R. Benjamin, "Direction Finding System Using Symmetric-Pair Antenna Arrays," *IEEE Proceedings on Radar, Sonar, and Navigation,* Vol. 142, No. 3, pp.130-136, June 1995.

[6] P. E. Pace, D. Styer, I. A. Akin, "A Folding ADC Preprocessing Architecture Employing a Robust Symmetrical Number System With Gray-Code Properties," *IEEE Transactions on Circuits and Systems,* Vol. 47, No. 5, pp.462-467, May 2000.

[7] Charles F. Babb, "Mixed Signal Processor for a Robust Symmetrical Number System Direction Finding Antenna," Master's Thesis, Naval Postgraduate School, Monterey, California, September 2002.

[8] Kevin Kwai, "An Analysis of Three-Channel RSNS Virtual Spacing Direction Finding System," Master's Thesis, Naval Postgraduate School, Monterey, California, December 2007.

[9] Brian L. Luke, Phillip E. Pace, "N -Sequence RSNS Ambiguity Analysis," *IEEE Transactions on Information Theory,* Vol. 53, No. 5, pp.1759-1766, 2007.

[10] B. L. Luke, P. E. Pace, "*N* Sequence RSNS Redundancy Analysis," 2006 *IEEE International Symposium on Information Theory,* pp.2744-2748, July 2006.

[11] Jui-Chun Chen, "A Virtual RSNS Direction Finding Antenna System," Master's Thesis, Naval Postgraduate School, Monterey, California, December 2004.

[12] David Jenn, “RSNS Direction Finding Array,” Status Report, Naval Postgraduate School, Monterey, CA, September 2008.

[13] Burgstaller, G., “Wirelessly Networked Digital Phased Array: Design and Analysis of a 2.4GHz Demonstrator,” Master’s Thesis, Naval Postgraduate School, Monterey, California, September 2006.

[14] Analog Devices web page: www.analog.com. 0.8 GHz – 2.7 GHz Direct Conversion Quadrature Demodulator, AD8347 Specification Sheet.

[15] National Instruments web page: www.ni.com. See NI Developer Zone and search for 5112 synch.

[16] Stephanie Bay, Benoit Geller, Alexandre Renaux, Jean-Pierre Barbot, and Jean-Marc Brossier, “On the Hybrid Cramér Rao Bound and Its Application to Dynamical Phase Estimation,” *IEEE Signal Processing Letters,* pp.453-456, 2008.

INITIAL DISTRIBUTION LIST

1. Defense Technical Information Center
   Ft. Belvoir, Virginia

2. Dudley Knox Library
   Naval Postgraduate School
   Monterey, California

3. Chairman, Code ECE
   Naval Postgraduate School
   Monterey, California

4. Prof. Phillip E. Pace
   Department of Electrical & Computer Engineering
   Naval Postgraduate School
   Monterey, California

5. Prof. David C. Jenn
   Department of Electrical & Computer Engineering
   Naval Postgraduate School
   Monterey, California

6. LCDR Christopher M. Guoan, USN
   Advanced Concepts and Demonstrations
   Navy Information Operations Command Suitland, Maryland

7. Mr. John Kato
   Naval Network Warfare Command (NETWARCOM)

8. Dr. Brian Luke
   CCSG-10, N3

9. Mr. Al Di Mattesa
   NRL code 5701
   Washington D.C.

10. Dr Peter Craig
    ONR code 312
    Washington D.C.